aerospace

MDPI

*Article*

# Results of the H2Avia Project: Potential of Hydrogen for Global Aviation

**Fabian Nicolas Peter [1,*], Marc Engelmann [1], Meriem Fikry [1], Michael Lüdemann [1], Leonard Moser [1], Christopher Warsch [1], Rafael Balderas-Xicohtencatl [1], Adnan Muslić [1], Elif Erden [1], Mirko Hornung [1], Tobias Welsch [2], Florian Schültke [2], Eike Stumpf [2], Samarth Kakkar [3], Wolfgang Heinze [3], Matthias Haupt [3], Rolf Radespiel [3], Vivian Kriewall Peters [4], Thimo Bielsky [4], Frank Thielecke [4], Nicolas Moebs [5] and Andreas Strohmayer [5]**

[1] Bauhaus Luftfahrt e.V., Willy-Messerschmitt-Straße 1, 82024 Taufkirchen, Germany
[2] Institute of Aerospace Systems, RWTH Aachen University, Templergraben 55, 52062 Aachen, Germany
[3] Institut für Flugzeugbau und Leichtbau, Technische Universität Braunschweig, Universitätsplatz 2, 38106 Braunschweig, Germany
[4] Institut für Flugzeug-Systemtechnik, Hamburg University of Technology, Am Schwarzenberg-Campus 1, 21073 Hamburg, Germany
[5] University of Stuttgart, Institute of Aircraft Design, Pfaffenwaldring 31, 70569 Stuttgart, Germany
* Correspondence: fabian.peter@bauhaus-luftfahrt.net

**Abstract**

This paper presents an integrated assessment of liquid hydrogen as an aviation energy carrier, covering fuel production, aircraft performance, and fleet-level climate impacts. The results, based on the H2Avia research project, indicate substantial potential for reducing life-cycle global warming impacts compared to conventional kerosene. The analyses conducted for the interdisciplinary assessment are presented. The analysis shows that the use of liquid hydrogen eliminates $CO_2$ emissions during fuel burn, resulting in a significant reduction in global warming potential compared to conventional kerosene, despite remaining upstream emissions from production and transport. The aircraft application cases and the applied technologies assessment scenario are described. The modeled technologies essential for the hydrogen aircraft are discussed, and exemplary values are given. Integrated overall aircraft performance results are given and discussed. At the aircraft level, hydrogen-based aircraft require an 8–18% increase in design mission block energy compared to a 2040 kerosene baseline yet still achieve a reduction in effective global warming potential of 55–86% comparing a representative pair route between Europe and North America (6730 km). An overview of the fleet modeling approach and the applied scenarios is given. For a scenario with energy cost and climate impact as equally weighted minimization goals, the global fleet analysis yields a global warming potential reduction of 60% compared to the non-liquid hydrogen baseline scenario. Overall, the results suggest that liquid hydrogen-powered aircraft can deliver significant mission- and fleet-level reductions in global warming potential and thus represent a promising pathway for achieving long-term aviation climate targets.

**Keywords:** hydrogen aviation; aviation climate impact; hydrogen aircraft design; life-cycle assessment; fleet modeling; future scenarios



Academic Editor: Konstantinos Kontis

Received: 17 April 2026
Revised: 2 June 2026
Accepted: 2 June 2026
Published: 12 June 2026

## 1. Introduction

The research project "H2Avia—Hydrogen in Aviation" [1–3] was motivated by aviation's need to limit its impact on global warming. As the primary energy source for regional, short-haul, and long-haul aircraft, liquid hydrogen ($LH_2$) is currently one of the most attractive long-term technology options. The feasibility of $LH_2$ as an energy carrier for aviation has been investigated for several decades. The proof of concept was delivered in 1988 with the hydrogen-powered flights of the Tu-155 experimental aircraft (see Sosounov and Prlov 1990 [4]). Foundational research was presented by Brewer (1991) [5], analyzing the feasibility of $LH_2$ for a long-range commercial application and assessing basic cost and climate aspects. Brewer found that the usage of $LH_2$ in commercial aircraft is technically feasible. The European Union research project CRYOPLANE (2003) [6] considered a wide range of aircraft application sizes and considered basic cost and climate performance as well, concluding that $LH_2$-powered aircraft may exhibit increased energy demand and strongly reduced climate impact and might become cost competitive in 2040. However, many assumptions and models of CRYOPLANE are outdated by now, such as assuming fossil-based pathways as the primary source for $LH_2$. The recent literature has significantly advanced the knowledge on critical components of $LH_2$ aircraft, such as the tank, e.g., by Huete and Pilidis (2021) [7], as well as the updated performance estimates for $LH_2$-powered aircraft, e.g., by Onorato et al. (2022) [8]. Progress has also been made for the propulsion by $LH_2$ combustion, as in the project ENABLEH2 and, e.g., its concepts for the treatment of cryogenic hydrogen before injection in the combustion chamber (see Patrao et al. (2024)) [9]. Furthermore, the scope of studies is increasing, as exemplified by Ramm et al. (2024) [10], taking into account environmental assessment based on global warming potential (GWP), demonstrating substantial climate impact reductions and potential economic viability compared to power-to-liquid (PtL) carbon-based sustainable aviation fuels (SAFs). Industry concepts currently under development, such as Airbus ZEROe [11] or Fokker Next Gen [12], indicate momentum but lack publicly available and scientifically peer-reviewed content. One of the most comprehensive recent research activities on the topic of $LH_2$ must be considered to be the FlyZero study by ATI (2022) [13], which displayed climate and commercial attractiveness of $LH_2$-powered concepts for different aircraft sizes. Despite these advances, most existing studies focus either on aircraft-level performance or basic environmental assessments, while comparatively few integrate hydrogen production, infrastructure, aircraft integration, fleet modeling, and climate impacts within a consistent framework and across all major aircraft sizes.

H2Avia extended the current research findings in two key aspects. First, they integrated the latest models and estimates for critical aircraft components such as propulsion, the cryogenic tank, and the fuel system and applied them to the main contributing aircraft sizes. Second, H2Avia elevated the environmental evaluation from basic $CO_2$ assessment to an integrated climate metric, i.e., GWP, and expanded the assessment to a holistic life-cycle assessment (LCA). This paper builds upon H2Avia's results to provide a holistic assessment of $LH_2$ as an aviation energy carrier by combining analyses of $LH_2$ production and distribution, aircraft technology integration, and fleet modeling for all major application cases and life-cycle-based climate impact assessment. Therefore, the following questions are addressed:

- To what extent do hydrogen production pathways and infrastructure assumptions influence overall climate performance?
- How do updated component weight penalties and integration constraints for $LH_2$ affect overall aircraft performance?
- How do operational uncertainties, particularly regarding aviation-induced cloudiness (AIC), affect the overarching LCA results?

- Are $LH_2$-powered aircraft economically competitive compared to SAF-powered alternatives?

The H2Avia project, therefore, adopts a holistic systems perspective encompassing hydrogen production, airport infrastructure, aircraft integration, and global fleet-level climate assessment. This multi-scale methodology enables a consistent evaluation of the technological, operational, environmental, and economic implications of $LH_2$-based aviation. The overall assessment framework applied within H2Avia is illustrated in Figure 1.


**Figure 1.** Overview of the H2Avia assessment framework covering hydrogen production pathways (**a**), airport infrastructure and aircraft integration (**b**), and fleet-level climate impact assessment (**c**).

## 2. Hydrogen Production and Logistics

### *2.1. Hydrogen Production and Transport*

After selecting representative supply scenarios for liquefied green hydrogen, the corresponding process chains were modeled. Subsequently, life-cycle inventories were created for the individual components, incorporating technological assumptions that considered a long-term time horizon regarding the key performance characteristics. Based on these inventories, an initial LCA was conducted for green hydrogen production at two locations, following the methodology described in [14]. The first scenario uses electricity produced via wind in the coastal region of Lettercamps (Ireland), while the other scenario uses electricity generated from solar power in Ouarzazate (Morocco). Figure 2a shows the mean wind speed at a height of 100 m for Lettercamps and the Global Horizontal Irradiation (GHI) for Ouarzazate [15,16], underlining the good prerequisites of the locations for wind and solar electricity production, respectively. The liquefied hydrogen was then assumed to be transported by ship to the selected airport in Frankfurt (Germany). Figure 2b shows that the GWP of production and transport of $LH_2$ at the solar location results in ca. 2.5-fold higher emissions than from the wind location, primarily due to the greater environmental impact of electricity generation (photovoltaic plant, ground mounting, photovoltaic modules, and inverter), which, in turn, mostly depends on the capacity factor of the respective electricity production technology. Using typical values for the carbon intensity (CI) of grid electricity in Europe, e.g., 363 g $CO_2$-eq./kWh for Germany, results in emissions far higher than those of conventional jet fuel production [17]. A CI value of around 205 g $CO_2$-eq./kWh roughly equals the emissions of conventional jet fuel, while in order to obtain a 70% reduction in GHG emissions compared to conventional jet fuel production, the CI of electricity input needs to be around 62 g $CO_2$-eq./kWh. The CI value of a typical nuclear power plant is roughly in the same range as renewable electricity production from PV and wind and therefore also results in similar GWP100 values for $LH_2$ production [18].

Table 1 presents a comparison between the GWP of $LH_2$ determined in this study and the literature values for alternative carbon-based SAF production pathways, such as hydroprocessed esters and fatty acids (HEFA) and Alcohol-to-Jet (AtJ). The scope of the present LCA is focused on $CO_2$-equivalent emissions arising from hydrogen production, liquefaction, and transport to the airport. For consistency with conventional fuel life cycle, the combustion phase is represented only by direct $CO_2$ emissions, given in g$CO_2$

equivalents per megajoule (MJ) of fuel. Non-$CO_2$ effects from aircraft operation are not considered within this LCA because they require a separate atmospheric impact assessment methodology; these effects are therefore evaluated independently in Section 5.1. The comparison reveals that the production and transportation of $LH_2$ has, on average, a lower impact than all other pathways, including SAFs produced via the PtL Fischer–Tropsch (FT) pathway.

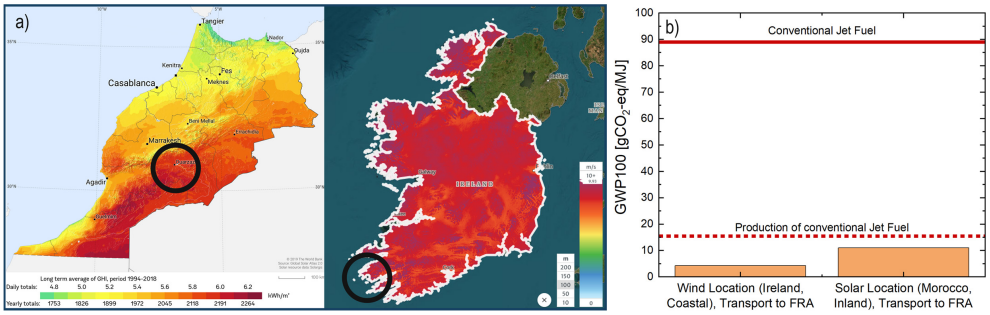


**Figure 2.** Two selected hydrogen production sites with wind speed and HI (**a**) with their respective comparison of GWP (**b**).

**Table 1.** Comparison of the GWP values of various fuel pathways.

| Pathway | GWP Production [$gCO_2$-eq/MJ] | $CO_2$ Emissions During Combustion [$gCO_2$/MJ] |
|---|---|---|
| $LH_2$ this study | 4.3–11.0 | 0 |
| PtL (FT, [19–21]) | 5.0–21.4 | 0 |
| HEFA ([22]) | 13.9–47.4 | 0 |
| AtJ ([22]) | 23.8–65.7 | 0 |
| Conventional jet fuel ([22]) | 15.5 | 73.5 |

Compared to conventional jet fuel, which has combined emissions of 89.0 $gCO_2$-eq/MJ primarily due to the combustion of fossil carbon, $LH_2$ can achieve a substantial reduction in emissions of more than 85%, depending on the production pathway. A more detailed LCA, including the contributions of the individual process steps of production, liquefaction, and transport, is described in Section 5 and used for further quantitative considerations of the energy carrier, which will play a key role for the holistic assessment.

### *2.2. Airport Logistics*

To address hydrogen distribution on airport premises, a literature review was conducted on storage and distribution concepts, focusing on minimizing losses based on delivery quantity and form. Building on this, a distribution network was designed to transport hydrogen from large central storage tanks to individual refueling points at the aircraft, either via truck or pipeline [23]. Two airports were selected as case studies: Frankfurt (FRA) airport, representing a large hub, and Bremen (BRE) airport, representing a smaller airport (Figure 3). A detailed techno-economic assessment of the $LH_2$ infrastructure was outside of scope of the present study. However, the selected infrastructure is consistent with the findings of Hoelzen et al. [24], who showed that truck-based $LH_2$ refueling systems are economically favorable for airports with low hydrogen demand, whereas pipeline and hydrant systems become advantageous at larger airports with high $LH_2$ throughput. Their analysis further indicates that the refueling infrastructure itself contributes only approximately 3–4% of the total $LH_2$ supply cost, with hydrogen production and liquefaction dominating the overall economics [24].

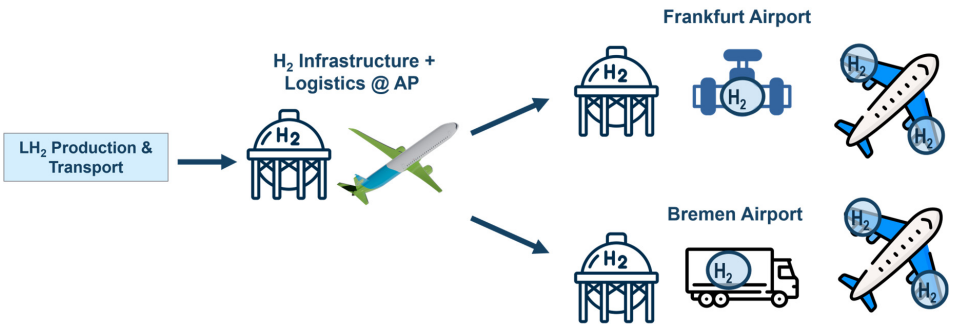


**Figure 3.** Airport distribution concepts comparison for different airport sizes.

Based on these findings, airport-specific $LH_2$ infrastructure concepts were developed for Bremen and Frankfurt airports. Parameter and capacity studies were carried out to refine the network design, and hydrogen-specific refueling systems were defined in compliance with safety regulations, including a detailed description of a safe and efficient refueling process. The results indicate that the optimal distribution method depends on airport size: the truck-based distribution is suitable for smaller airports such as Bremen, while pipeline-based distribution offers advantages for large-scale airports such as Frankfurt due to higher hydrogen demand and throughput. Although the Frankfurt scenario primarily relies on a pipeline/hydrant distribution system, limited use of tank trucks may still be required for operational flexibility, redundancy, and maintenance. These are not included in the present assessment due to their expected minor contribution relative to the overall hydrogen throughput. Based on the areal dimensions of the exemplary airports, the total pipeline length at Frankfurt airport was taken as 1500 m, and the average truck driving distance was assumed to be 1800 m. Particular emphasis was placed on minimizing boil-off losses and ensuring safe and efficient refueling operations. Key results are summarized in Table 2.

**Table 2.** Results of the hydrogen distribution concept study at exemplary airports.

| Parameter | Unit | Frankfurt | Bremen |
|---|---|---|---|
| Number of aircraft per day | - | 504 | 15 |
| Assumed liquid hydrogen required | t/day | 2127 | 34 |
| Number of liquid hydrogen storage tanks | - | 8 | 1 |
| Total pipeline length | m | 1500 | - |
| Number of pipelines | - | 5 | - |
| Number of tank trucks | - | - | 3 |

In addition, the simulation of the ground infrastructure showed that boil-off losses remain small at both airports but differ in their distribution and recoverability. At FRA, the total boil-off amounts to approximately 0.8% of the delivered $LH_2$, of which roughly one quarter is recoverable, resulting in an effective loss of approximately 0.6%. At BRE, the total boil-off is higher at approximately 1.8%, with an effective loss of 1.5%, attributable to the truck-based distribution where each filling cycle requires cooling of the truck tank, producing non-recoverable boil-off (28% of total).

In the present ground infrastructure model, the boil-off gas from the storage tanks and from the aircraft tanks during refueling is assumed to be recovered. Recovery pathways include re-compression and utilization in a stationary fuel cell for on-site power generation or collection and sale as gaseous hydrogen [25]. The truck boil-off at BRE is assumed to be non-recoverable due to the transient nature of the filling process. For the aircraft in flight, any boil-off is assumed to be vented (see Section 3.3), as on-board re-liquefaction would drastically increase system complexity. A more detailed optimization of BOG recovery

systems, analogous to the dynamic terminal modeling approaches applied in $LH_2$ export terminal studies [26], is recommended as future work.

## 3. Hydrogen Aircraft Technologies

### *3.1. Technology Assessment Scenario*

The aircraft technology selection in H2Avia aimed to provide a solid basis for assessing the potential of hydrogen in aviation. The scope of the study was limited to aircraft sizes with major impact on global aviation emissions, represented by three aircraft categories and their projected configurations for 2040. The Airbus A220-100, A320neo, and A350-900 are the reference platforms. Subsequently, analogous aircraft were designed and designated as regional (REG-REF), short–medium-range (SMR-REF), and long-range reference (LR-REF). A second criterion was established to define a technology scenario enabling a fair and robust comparison between future kerosene (or SAF)-powered aircraft and their hydrogen equivalents. For this, the reference aircraft were taken as basis for the incorporation of a set of evolutionary technologies, e.g., incremental mass savings or engine performance improvements. These evolutionary technologies were integrated to achieve a realistic application case for the envisaged entry into service (EIS) of 2040 and produce the baseline aircraft (REG-BAS, SMR-BAS, and LR-BAS). A third criterion was to prioritize technically mature, low-risk technologies for the hydrogen aircraft. This meant, where possible, selecting proven options (e.g., propulsion) over potentially higher performing but less mature alternatives. Afterwards, these elementary H2-technologies (e.g., $LH_2$ storage) were defined, which represent highly likely/low-risk $LH_2$ configurations (e.g., tube and wing, engine on wing, etc.). By integrating this set of technologies into the baseline aircraft, the hydrogen aircraft (REG-H2, SMR-H2, and LR-H2) were derived. The comparison of the baseline and elementary technology hydrogen aircraft was the focus of the technological assessment in H2Avia. This approach is depicted in Figure 4.

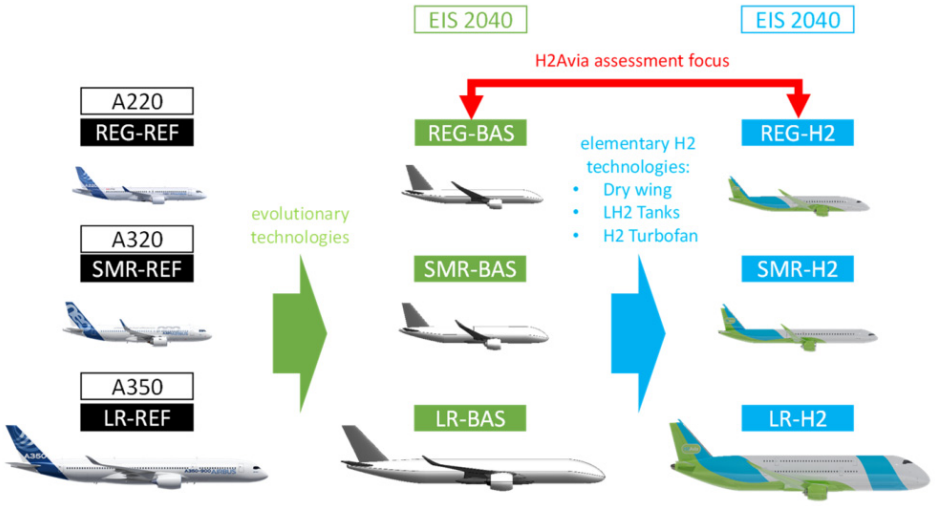


**Figure 4.** H2Avia technology assessment scenario [3].

### *3.2. Propulsion*

The propulsion systems for the three aircraft generations (REF, BAS, and H2) and classes (REG, SMR, and LR) were sized according to a methodology aligned with the defined assessment focus. The reference aircraft employ the reference engine performance decks from RWTH Aachen University [27–29]. For the baseline aircraft, a dedicated set of engines was derived to enable a better resolved basis for the subsequent switch to hydrogen. The baseline engines, which represent a technology status of 2040, feature twin-shaft drive architectures with a high-speed low-pressure turbine and reduction gears

for the fan. Existing heuristics for the design of the propulsion system in the model, such as turbo component effective loading determination, turbo machinery Reynolds number correction, or turbine cooling mass flow calculations, were adapted for use with hydrogen gas turbines. Data for fuel consumption and thrust were provided for the conceptual aircraft design. For all studies, the following fuel heating values were considered [30,31]:

- Kerosene: 42.77 MJ/kg;
- Hydrogen: 120.07 MJ/kg.

Thermodynamic studies were carried out to identify the optimum operating point for the design of the individual baseline and hydrogen engines. To this end, the turbine inlet temperature (T4) and the overall pressure ratio were varied to find the operating point with the lowest specific fuel consumption. The geometric design of the engine takes place at the operating point top of climb (ToC). Afterwards, the designed propulsion system is further investigated in off-design studies. Figure 5 shows the specific fuel consumption for various combinations of T4 and the overall pressure ratio (OPR) for the SMR-H2 engine design, also giving the result for the bypass ratio (BPR). The thrust specific fuel consumption (TSFC) is represented as shell curves. The minimum design TSFC needs to be found for the design point inside the highlighted limits for the compressor outlet temperature (T3), T4, and the inter turbine temperature (T45) at take-off. Those limits are mostly driven by the maximum material temperatures. The flow path sizing point is defined at maximum climb (MCL) at ToC with a Mach number of 0.78, an altitude of 35,000 ft, a deviation from the International Standard Atmosphere (ISA) by +10 K, and a design net static thrust ($FN_{ST}$) of 23 kN. The considered take-off point for the determination of the limits for T3, T4, and T45 is chosen at a Mach number of 0.2, sea level (SL), ISA deviation of +15 K, and a net static thrust of 102 kN. Once the minimum TSFC is found, the corresponding T4 and OPR define the design point chosen at ToC. For the SMR-H2 application the point is defined at an OPR of 52 and a turbine inlet temperature of 1650 K.

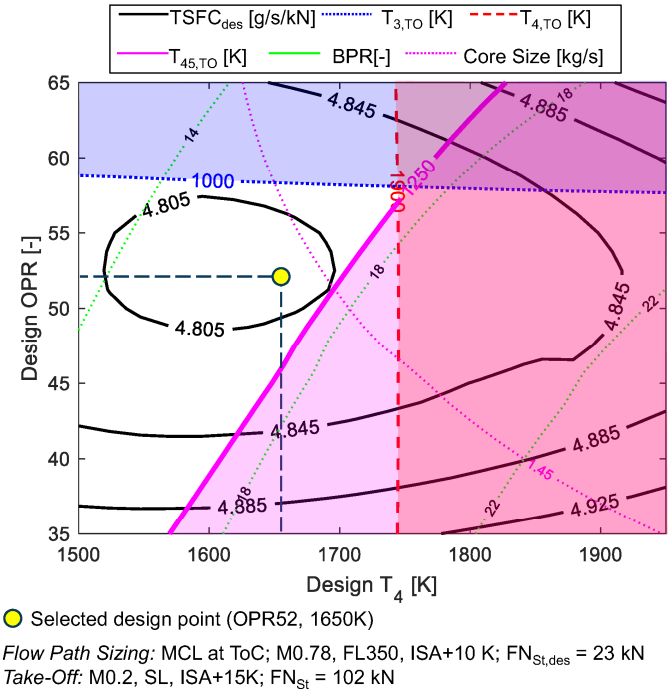


**Figure 5.** Multi-point design optimization study (T4-OPR) for the SMR-H2 engine.

The $NO_x$ emissions were calculated on the basis of the DLR Fuel Flow Method [32]. For this purpose, the fuel consumption of the engine is calculated for reference conditions so that the $NO_x$ emission index at the reference point ($EI_{NOx,ref}$) can be determined based

on the dependency in Figure 6. This is used to determine an emission index for the specific flight altitude, which can then be calculated with the fuel consumption from the engine performance calculation to $NO_x$ emissions in $g_{NOx}/s$. Improved and further developed combustion chamber technologies are considered using a technology factor. Based on Sáez Ortuño et al., $NO_x$ emission indices are developed for hydrogen engines [33]. Overall, this leads to a reduction in the $NO_x$ emission index of 18%, as well as a further reduction in total $NO_x$ emissions due to a reduced hydrogen fuel flow.

Table 3 lists the main propulsion performance parameters of the H2 concepts in comparison to the BAS applications for each aircraft type considered. Design parameters such as, e.g., OPR and BPR were identified for these engines with the above-mentioned multi-point design optimization. The thrust specific power consumption (TSPC) [34] is a suitable parameter to compare the engines' efficiency. The TSPC improvements of the H2 engines vs. the BAS engines range from 2 to 3%.

**Table 3.** Comparison of key propulsion characteristics for the BAS and the H2 concepts for the REG, SMR, and LR aircraft.

| | **Unit** | **Take-Off** | | **Top of Climb** | | **Cruise** | |
|---|---|---|---|---|---|---|---|
| | | | | REG | | | |
| | | BAS | LH2 | BAS | LH2 | BAS | **LH2** |
| Flight altitude | m | 0 | 0 | 10,668 | 10,668 | 10,668 | 10,668 |
| Mach number | - | 0.20 | 0.20 | 0.78 | 0.78 | 0.78 | 0.78 |
| ISA deviation | K | +15 | +15 | +10 | +10 | 0 | 0 |
| Thrust | kN | 88.7 | 88.7 | 20.0 | 20.0 | 18.0 | 18.0 |
| Bypass ratio | - | 14.0 | 15.1 | 14.7 | 15.9 | 15.1 | 16.3 |
| Overall pressure ratio | - | 43.4 | 43.2 | 50.0 | 50.0 | 47.1 | 47.0 |
| Thrust specific fuel consumption | g/(kNs) | 8.37 | 2.88 | 13.86 | 4.81 | 13.51 | 4.67 |
| Thrust specific power consumption | W/N | 358 | 353 | 593 | 578 | 578 | 561 |
| NOx emission index | $g_{NOx}/kg_{fuel}$ | 23.8 | 19.5 | 12.8 | 10.5 | 11.0 | 9.0 |
| NOx emissions | $g_{NOx}/s$ | 17.7 | 5.0 | 3.6 | 1.0 | 2.7 | 0.8 |
| | | | | SMR | | | |
| | | BAS | LH2 | BAS | LH2 | BAS | LH2 |
| Flight altitude | m | 0 | 0 | 10,668 | 10,668 | 10,668 | 10,668 |
| Mach number | - | 0.20 | 0.20 | 0.78 | 0.78 | 0.78 | 0.78 |
| ISA deviation | K | +15 | +15 | +10 | +10 | 0 | 0 |
| Thrust | kN | 102.0 | 102.0 | 23.0 | 23.0 | 18.3 | 18.3 |
| Bypass ratio | - | 15.1 | 16.6 | 16.4 | 17.0 | 17.2 | 18.0 |
| Overall pressure ratio | - | 49.0 | 43.6 | 55.0 | 52.0 | 48.5 | 45.4 |
| Thrust specific fuel consumption | g/(kNs) | 8.62 | 2.76 | 13.82 | 4.78 | 13.42 | 4.75 |
| Thrust specific power consumption | W/N | 369 | 331 | 591 | 574 | 574 | 570 |
| NOx emission index | $g_{NOx}/kg_{fuel}$ | 22.7 | 18.8 | 12.3 | 10.1 | 8.8 | 7.2 |
| NOx emissions | $g_{NOx}/s$ | 19.9 | 5.4 | 3.9 | 1.1 | 2.2 | 0.6 |
| | | | | LR | | | |
| | | BAS | LH2 | BAS | LH2 | BAS | LH2 |
| Flight altitude | m | 0 | 0 | 10,668 | 10,668 | 10,668 | 10,668 |
| Mach number | - | 0.200 | 0.200 | 0.825 | 0.825 | 0.85 | 0.85 |
| ISA deviation | K | +15 | +15 | +10 | +10 | 0 | 0 |
| Thrust | kN | 333.0 | 333.0 | 75.0 | 75.0 | 60.0 | 60.0 |
| Bypass ratio | - | 12.2 | 13.3 | 12.3 | 13.4 | 12.6 | 13.7 |
| Overall pressure ratio | - | 53.5 | 53.3 | 60.0 | 60.0 | 52.4 | 52.2 |
| Thrust specific fuel consumption | g/(kNs) | 8.65 | 2.98 | 14.8 | 5.13 | 13.8 | 4.81 |
| Thrust specific power consumption | W/N | 370 | 358 | 631 | 616 | 590 | 577 |
| NOx emission index | $g_{NOx}/kg_{fuel}$ | 47.9 | 39.3 | 30.0 | 24.6 | 17.7 | 14.9 |
| NOx emissions | $g_{NOx}/s$ | 138.0 | 39.0 | 33.6 | 9.6 | 14.8 | 4.2 |

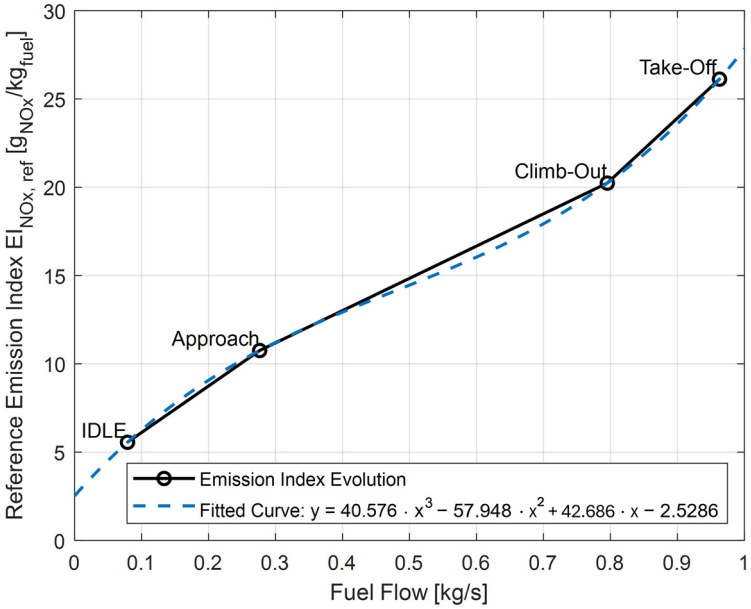


**Figure 6.** Determination of the reference $NO_x$ for the calculation of $NO_x$ emissions using the DLR Fuel Flow Method [32].

### *3.3. Hydrogen Fuel System*

The introduction of a hydrogen fuel system represents a fundamental architectural change compared to conventional aircraft. To maximize volumetric storage density, hydrogen is stored in liquid form at cryogenic temperatures and elevated pressures, requiring spherical or cylindrical pressure vessels. Due to their geometry, these tanks cannot be integrated into the wing structure feasibly. Consequently, airframe integration of $LH_2$ tanks becomes a primary design challenge. Furthermore, the distribution lines must be routed from the fuselage to the engines on the wings, encountering stringent spatial constraints. These routing paths must ensure segregation from other on-board systems (OBSs), such as electrical power supplies, to meet safety and certification requirements.

The baseline layout of the $LH_2$ supply system's architecture in the scope of H2Avia is depicted in Figure 7. It consists of two tanks, two cold boxes, and distribution pipes feeding the engines. It is assumed that hydrogen is distributed in liquid form from the storage to the consumer systems, i.e., engines and the $H_2$-powered auxiliary power unit (APU), neglecting any heat ingress by equipment such as pumps. In nominal operation, each tank feeds a single engine, with a cross-feed capability available for off-nominal scenarios. The $LH_2$ conditioning subsystems are assumed to be in the engine vicinity [9], utilizing waste heat to contribute to the vaporization of hydrogen. While this thermodynamic process and the mass estimation of any required heat exchangers are outside the scope of the present study, it is noted that (beyond thrust generation) the $H_2$-powered turbofans provide non-propulsive power (electric and hydraulic with no bleed air off-takes) to the various OBSs.

In addition to the design of the $LH_2$ system itself, additional operational constraints must be considered. These include, among other things, the management of boil-off gases, which are inevitably generated by heat input to the system, particularly to the tanks. However, in the scope of this study, boil-off emissions during normal ground and flight operations are assumed to be negligible, provided the thermal insulation performance of the hydrogen tanks is sufficient. This aspect is taken into account in the design of the $LH_2$ tanks (cf. Section 3.4.1). Should abnormal venting be required during extended ground operations, the boil-off gases are assumed to be released into the environment. Liquefying

the boil-off gases on board the aircraft would drastically increase system complexity and, thus, is not feasible.

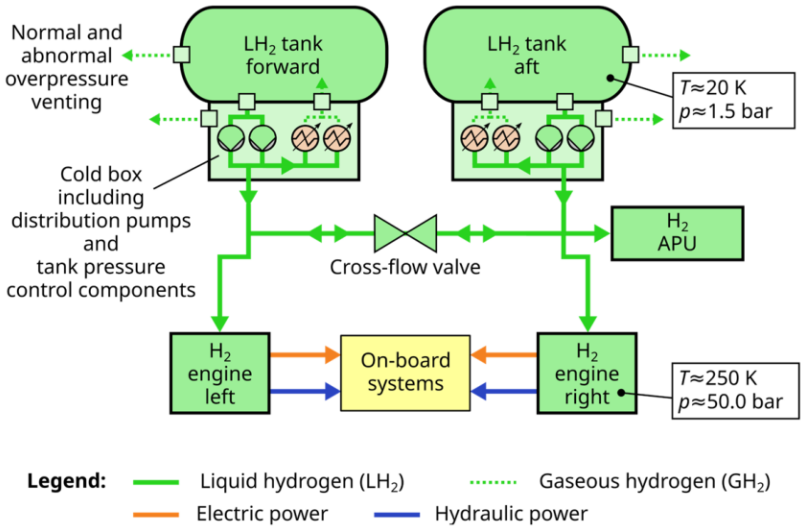


**Figure 7.** Baseline architecture of the $LH_2$ supply system.

A critical uncertainty remains regarding the dynamic heat input introduced by system components such as cryogenic pumps and valves during operation. Cryocoolers in the vicinity of the tank and other equipment could enable the reduction of system-internal boil-off [35]. If this localized heat input leads to localized boiling, a two-phase LH2/GH2 fluid may form. To avoid venting this boiled-off hydrogen into the atmosphere, the system architecture should ideally be able to handle the two-phase mixture and lead it to the downstream consumers for final conditioning and utilization. Consequently, for now, the on-board venting system is treated strictly as an emergency safety feature to mitigate abnormal overpressure events or to facilitate system purging. In general, a more detailed examination of boil-off mechanisms should be conducted in the future as part of detailed system design studies, for example, using dynamic simulation approaches [26].

#### 3.3.1. Conceptual Sizing and Evaluation Methodology

The $LH_2$ supply system, including the tanks and the distribution pipes, is sized as part of the conceptual design phase. To this end, the established overall systems design (OSD) framework developed at the Institute of Aircraft Systems Engineering at Hamburg University of Technology was applied (Figure 8) [36–39]. The framework comprises two key methodologies: the systems architecting assistant (*SArA*) for the model-based systems engineering-driven generation and evaluation of a feasible functional–logical overall OBS architecture and *GeneSys* for the physical preliminary sizing of the OBS and its components. First, the common parametric aircraft configuration schema (CPACS) interface is used, which contains a parametric geometry description of the aircraft [40,41]. Based on the aircraft geometry, the topology of the OBS is automatically created (including the $LH_2$ supply system). Specifically, the systems' components are spatially positioned within the aircraft. Additionally, the connections between the components, such as cables, hydraulic pipes, or $LH_2$ pipes, are generated and positioned. In the process, the segregation of connections is considered as a boundary condition.

With the systems topology known, the graph-based sizing procedure is performed, taking the $LH_2$ pipe lengths into account. Here, the required thermodynamic properties and the mass flow of the consumers (e.g., engines) are propagated through the pipe network. Based on the required mass flow and power ratings, the individual $LH_2$ supply system

components (e.g., tank, cold box, pipes, pumps, heat exchangers, valves, and brackets) are sized based on response surface models and physics-based component scaling laws. The sizing results in terms of mass, center of gravity, and engine power off-take requirements are fed back to the overall aircraft design (OAD) discipline. The sizing results are generated and presented for the SMR-H2 and scaled according to the other concept aircraft relevant in the scope of H2Avia.

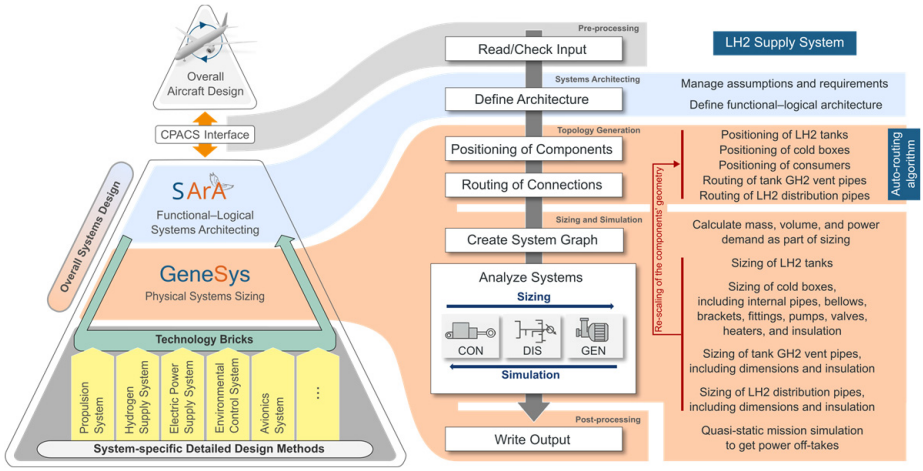


**Figure 8.** Overall systems design framework for conceptual on-board systems design, including $LH_2$ supply system sizing.

### 3.3.2. $LH_2$ Fuel Line Routing Concept and System Topology

For a low-wing aircraft, such as all aircraft considered in H2Avia, routing $LH_2$ supply lines from the fuselage tanks to the hydrogen turbofans located at the wings presents significant integration challenges. Especially compared to conventional kerosene fuel systems, where the energy carrier is typically stored in wing-integrated tanks and, thus, located near the wing-mounted engines. On a different note, for example, a fully electric powertrain or the placement of a fuel cell near the $LH_2$ tanks would also have the advantage of eliminating the need to run long cryogenic lines through the aircraft.

The routing path of the considered $LH_2$ supply lines conflicts geometrically with the passenger cabin and over-wing emergency exits or compromises aerodynamic performance, since routing lines through the pressurized cabin is judged to be unsafe, as any leakage would expose passengers to a hazardous flammable atmosphere. Furthermore, internal routing above the cabin (crown area) is considered unfeasible; accommodating the pipes would disrupt the fuselage's optimized oval cross-section, necessitating substantial structural reinforcement to maintain load-path continuity and prevent local instability. Within the wing area, pipes should be routed inside or along the spars wherever feasible, as these provide fixed attachment points for the pipes, like for hydraulic lines. In the context of a possible leakage, maximum distances of the $LH_2$ pipes to other system installations, especially high-voltage cables, must be maintained [42].

The SMR-H2 baseline adopts a lower fuselage routing configuration. Originating from the aft tanks, the distribution lines emerge from the lower rear fuselage and traverse externally toward the wing box via the shortest possible path. While aerodynamic fairings are requisite to shield the $LH_2$ pipes, the associated drag penalty is anticipated to be minimal. However, this requires further analysis in future work and is not part of the present paper. The resulting routing concept as an output from the OSD framework's topology generation procedure is shown in Figure 9.

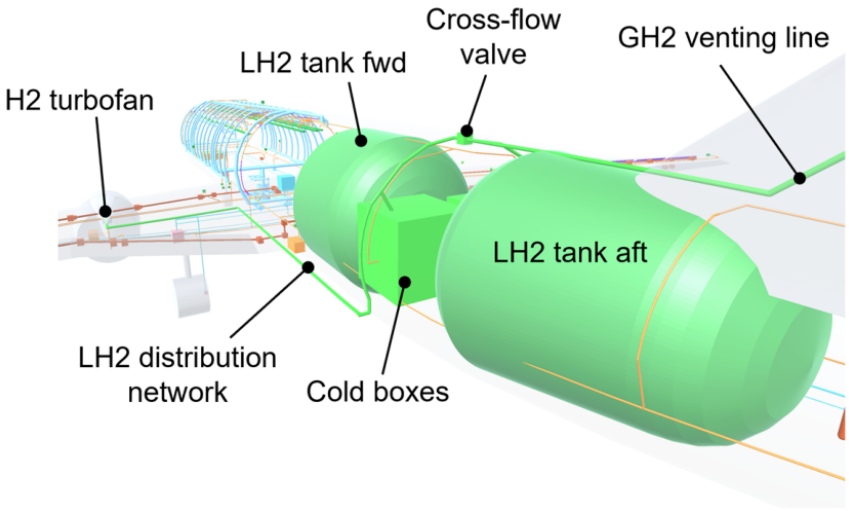


**Figure 9.** Topology of the $LH_2$ supply system and its components for the SMR-H2 concept aircraft.

A primary advantage of the depicted lower routing concept is the elimination of fairings transverse to the freestream. However, this configuration introduces a potential conflict regarding available installation space between the $LH_2$ pipes and the rear emergency slides. This needs to be analyzed in future work in the scope of a detailed design study. The routing of the gaseous hydrogen ($GH_2$) venting pipes is relatively straightforward and not subject to detailed analysis. The $GH_2$ venting lines run from the tanks along the leading edge of the vertical stabilizer, with the outlet located at its top. This ensures that gaseous hydrogen is vented at the highest point of the airframe, preventing any impingement on downstream aircraft surfaces. Given the known system topology, the conceptual sizing is performed according to Figure 8 and the sizing results of the $LH_2$ supply system are presented as follows:

#### 3.3.3. Conceptual Sizing Results of the $LH_2$ Supply System

By taking appropriate assumptions and input parameters into account, mass, center of gravity positions, and required engine power off-takes of the OBS are calculated based on physics-based component sizing and mass estimation laws. These laws are derived from data sheets of existing, similar components or based on high-fidelity analyses. Table 4 lists exemplary assumptions for the conceptual sizing process of the $LH_2$ supply system. The internal temperature of the cold box is assumed to be 20 K, consistent with the storage tank conditions [43]. Aerogel is utilized as the primary insulation, leveraging its high effectiveness in minimizing heat boil-off within the liquid hydrogen temperature range. The assumed installation factor accounts for the volumetric inefficiency within the cold box, reflecting the portion of the volume that cannot be utilized for active components. The burst pressure safety factor for the pipes accounts for normal and abnormal dynamic fluctuations in pressure and is chosen based on engineering judgement.

Table 5 depicts selected sizing results of the $LH_2$ supply system, i.e., cold boxes and pipes, exemplary for the SMR-H2. The stated geometry parameters are calculated based on the assumptions listed in Table 4, e.g., the pipe diameters are calculated based on the $LH_2$ mass flow rate. The integration and design of the tanks are discussed in depth in the following section. In general, the adoption of hydrogen propulsion architecture is expected to result in a system mass penalty compared to conventional aircraft. However, a comprehensive assessment must prioritize overall energy efficiency and the associated environmental impact.

**Table 4.** Assumptions for the sizing of the LH2 supply system.

| | Parameter | Unit | Value |
|---|---|---|---|
| Cold box | Internal temperature | K | 20 |
| | Insulation type | - | Aerogel |
| | Insulation thickness | m | 0.1 |
| | Installation factor | - | 2 |
| | $GH_2$ target temperature | K | 353 |
| Distribution and venting pipes | $LH_2$ max. mass flow rate per engine | kg/s | 0.3 |
| | $LH_2$ flow velocity | m/s | 9 |
| | $GH_2$ flow velocity | m/s | 20 |
| | Distribution nominal pressure | bar | 3 |
| | Burst pressure safety factor | - | 1.5 |
| | Distribution pipe interspace filling | - | Vacuum |
| | Material inner pipe | - | Stainless steel |
| | Material outer pipe | - | Stainless steel |
| | Interspace pressure | bar | $1 \times 10^{-8}$ |
| | Venting pipe interspace filling | - | Nitrogen |

**Table 5.** Exemplary mass and geometry sizing results of the $LH_2$ supply system for the SMR-H2.

| | Parameter | Unit | Value |
|---|---|---|---|
| 2 × cold box (forward and aft) | Electric power for $LH_2$ pumps and tank pressure management (both) | kW | 25.3 |
| | Outer diameter (each) | m | 1.5 |
| | Length (each) | m | 0.82 |
| | Volume (each) | $m^3$ | 0.71 |
| | Mass (both) | kg | 554 |
| Distribution pipes | Total length | m | 82 |
| | Outer pipe diameter | mm | 70 |
| | Inner pipe diameter | mm | 30 |
| | Mass | kg | 557 |
| Venting pipes | Total length | m | 23 |
| | Outer pipe diameter | mm | 76 |
| | Inner pipe diameter | mm | 48 |
| | Mass | kg | 190 |

### *3.4. Fuselage Design and Hydrogen Tank Integration*

The cabin and fuselage designs were first introduced for the three baseline aircraft (REG-BAS with 120 passengers, SMR-BAS with 180 passengers, and LR-BAS with 325 passengers), each updated to a projected 2040 technology level. Subsequently, initial hydrogen fuselage concepts were derived from these baselines following the workflow shown in Figure 10. These concepts represent the starting point for the OAD and the detailed fuselage mass calculation of the project partners.

The transition from the kerosene-powered baseline designs to hydrogen fuselage configurations was carried out using the Bauhaus Luftfahrt aircraft design environment (*BLADE*) [45] modules cabin and fuselage design environment (*CAFE*) and hydrogen tank design routine and assessment (*HyDRA*). They were used in a standalone version. The detailed fuselage and hydrogen tank design routine is based on the work of Engelmann et. al. [46]. The aircraft design loop requires an initial estimate for the required stored $LH_2$. From previous research work at Bauhaus Luftfahrt on $LH_2$ aircraft, a first-order estimate for energy need of $LH_2$ aircraft was derived. Specifically, this factor of increased required energy from a kerosene to an $LH_2$ aircraft was defined to be 1.2. This includes all major

effects as increase in the lower heating value of $LH_2$ as main driver of the engine fuel efficiency and structural impacts on the airframe as $LH_2$ tank mass. The final required $LH_2$ amount is afterwards determined in the design loop of the integrated aircraft design, providing a consistent design with regard to all aircraft components. The initial tank configurations are based on a down selection workshop presented at DLRK 2024 [44], in which configurations were selected for each of the three baseline aircraft [16]. For the REG-H2 and SMR-H2 aircraft, two tanks behind the cabin were selected as initial configuration, and for the LR-H2 aircraft, one tank in front and one behind the cabin. If the tank concepts had been applied to the baseline aircraft without adjusting the cabins, the fuselage geometries of the hydrogen variants would have fallen well outside the typical and reasonable range in terms of diameter-to-length ratio (slenderness ratio). For all aircraft variants, the cabin was therefore widened, and a second deck was added for the long-range variant. If the cabin had been widened with just one deck, there would have been a large dead space above the deck due to the larger diameter of the circle. This dead space can be significantly reduced by adding a second deck, and the cabin length is also significantly shortened. A second advantage of this widened fuselage cross-section is that the length of the hydrogen tanks can be reduced while maintaining the same volume, thereby improving the surface-to-volume ratio and the associated mass. The three initial hydrogen fuselage and cabin layouts are shown in Figure 11.

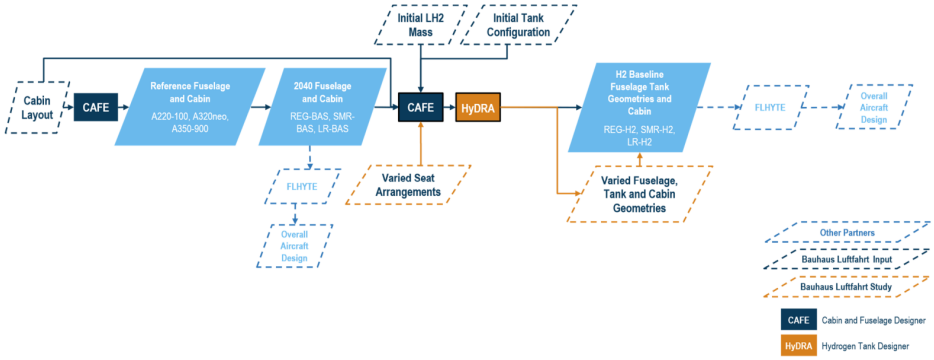


**Figure 10.** Fuselage design in the overall project context [44].

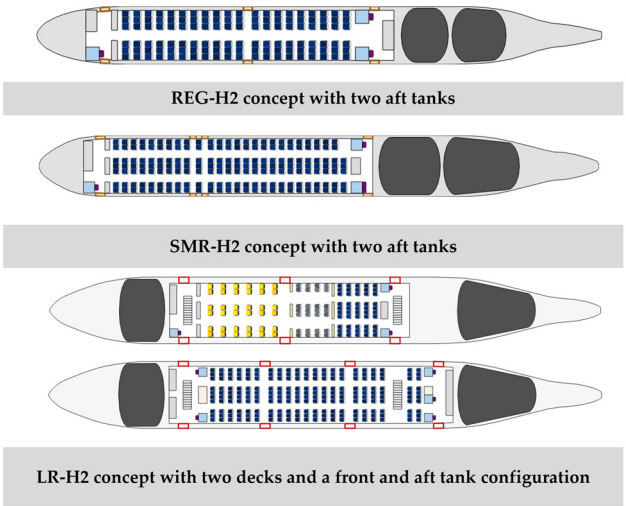


**Figure 11.** Overview of the three initial hydrogen fuselage concepts (adapted from [44]).

The initial geometries are subsequently investigated using the Python-based fuselage design and hydrogen tank integration tool environment (*FLHYTE*) developed by the University of Stuttgart. *FLHYTE* is intended to be released as an open-source tool

following publication of the present paper. To the authors' knowledge, no currently available open-source framework provides a comparable level of combined $LH_2$ tank modeling and quantification of integration-driven impacts on fuselage structural mass properties within an aircraft design loop. This deeper analysis is required because installation of cryogenic hydrogen tanks alters the fuselage architecture and load distribution compared with conventional kerosene aircraft, potentially requiring fuselage elongation or external fairings. These segments holding the tanks contain neither cabin furnishing nor floor installations and can be designed largely without cutouts (e.g., windows and doors), implying structural characteristics that deviate from those assumed in conventional empirical fuselage mass estimation methods. *FLHYTE* therefore combines a parametric $LH_2$ tank model with an explicit fuselage integration and structural sizing module so that the effects of tank placement and integration concept on fuselage geometry, mass, and center of gravity (CG) can be assessed within the aircraft design loop in a consistent manner.

Within the OAD loop, *FLHYTE* is used as an iterative higher-fidelity step between the initial hydrogen configuration synthesis and the next aircraft sizing iteration. It takes the current fuselage geometry, mission fuel demand, and installation assumptions as input, evaluates feasible tank and integration solutions, and returns updated geometry and mass properties to the aircraft-level process. The workflow applied in this study can be summarized as follows:

1. Input: baseline fuselage geometry, mission fuel demand, candidate tank locations, design pressure assumptions, integration constraints, and structural allowables.
2. Tank modeling: parametric tank sizing (geometry, structure, and insulation/thermal model), producing tank mass properties and performance indicators.
3. Integration and fuselage structural design: geometry modification (tank bays/fairings), load-path definition, and structural sizing under representative load assumptions.
4. Mass properties aggregation: component-level masses and CGs for fuselage structure and tank integration structures are combined into aircraft-level updates.
5. Data exchange and visualization: results are exported to standardized exchange formats (e.g., CPACS) and can be visualized for plausibility using parametric aircraft geometry modeling tools (e.g., TiGL Viewer from DLR).

#### 3.4.1. $LH_2$ Tank Modeling in *FLHYTE*

In *FLHYTE*, $LH_2$ tank modeling is carried out as a structured sizing workflow that starts from mission and installation requirements and determines a feasible tank geometry together with its structural mass, thermal behavior, boil-off, and aircraft-relevant mass properties. The workflow is designed to run either for a single design point or for large parametric sweeps so that alternative tank concepts and arrangements can be compared under consistent assumptions and constraints.

Tank sizing in *FLHYTE* starts from the mission $LH_2$ mass and converts it into a required storage volume using density at the assumed storage conditions, including ullage and unusable margins [5]. Potential tanks are represented parametrically as pressure vessel geometries (typically cylindrical or frustoconical vessels with domed heads) and are constrained by available fuselage space, clearances, and interface zones.

Structural sizing of the tank shell follows classical thin-walled pressure vessel theory, accounting for the different governing stress states in circular or elliptical shells and various vessel head geometries [5]. Design pressures are combined with material allowables at cryogenic temperature and suitable safety factors and margins to determine preliminary wall thickness requirements [5]. For vacuum-insulated double-wall tanks, the outer shell is subject to external pressure; hence, stability and buckling checks can become governing [47]. Local reinforcement allowances are applied at mounts and penetrations when required.

Thermal behavior is evaluated using a lumped, steady-state heat-ingress model based on an effective thermal resistance. In the nominal workflow, insulation thickness is iteratively sized to satisfy a predefined allowable mission boil-off and a minimum dormancy-time requirement; alternatively, a fixed insulation thickness can be prescribed and the resulting boil-off predicted. During normal flight operation, continuous fuel withdrawal is assumed to counteract heat-ingress-induced pressure rise so that boil-off leads to vented hydrogen loss only if the tank reaches the venting pressure threshold. The dormancy requirement primarily constrains extended ground phases, such as overnight parking. Parasitic heat leaks via supports and penetrations can be included via additive contributions. Boil-off is derived from an energy balance using latent heat, with either mission-time integration or a mission-average approximation.

The tank center of gravity is then determined consistently with the selected tank shape, orientation, and fill state, enabling direct coupling to aircraft trim, stability, and load distribution assessments. For concept comparison, *FLHYTE* reports performance indicators such as the gravimetric index (GI), defined as the ratio of usable hydrogen mass to the combined mass of stored hydrogen and the associated tank system; to ensure transparency, results can be reported with different scopes (e.g., tank only versus tank system), consistent with the current literature practice.

Finally, the predicted tank masses are calibrated against available data from existing $LH_2$ tanks. Since currently available reference data are dominated by tanks used in space applications, research-level designs, and demonstrator information, absolute mass predictions before calibration need to be interpreted with caution, as these systems follow partly different requirement sets and do not yet fully capture aviation-specific industrialization effects. Nevertheless, the calibrated results reproduce the range of GIs currently expected for aviation-relevant $LH_2$ tank concepts well. The methodology is explicitly set up to incorporate more representative datasets as they become available, which is expected to improve the accuracy of absolute mass predictions and the robustness of trade-off trends.

#### 3.4.2. Tank Integration and Fuselage Structural Design in *FLHYTE*

After the $LH_2$ tanks have been modeled, *FLHYTE* integrates the selected tank configuration into the aircraft by modifying the fuselage geometry according to the chosen integration concept. Depending on placement and volume utilization, this can include the elongation of the fuselage, the addition of external fairings, and the rearrangement of pressure bulkheads and locally adapted cross-sections. In contrast to conventional passenger aircraft fuselages, $LH_2$ tank segments may be structurally clean with reduced cutout density while simultaneously requiring dedicated interfaces for tank supports. This motivates an integration step in which the fuselage geometry is explicitly modified to accommodate the tanks, so that downstream structural sizing and the resulting mass properties (mass and CG) reflect the actual tank placement.

Hydrogen tanks induce concentrated masses and localized load introductions, which can substantially alter both local sizing drivers and global fuselage load distributions. *FLHYTE* therefore applies representative load assumptions capturing inertial effects (e.g., maneuvers or landing load factors), mount reaction forces, and their redistribution into the surrounding fuselage structure. The load-path modeling emphasizes that the structural impact is not driven by tank mass alone. It is strongly influenced by the way tank inertia loads are transferred into the fuselage and how these interfaces interact with the modified fuselage architecture (additional unpressurized bays, fairing junctions, or shifted bulkheads).

In the project, the integration concept shown in Figure 12 was adopted. The tanks are assumed to be supported only at the forward and aft suspensions, consistent with the polar mount concept in [48] and in contrast to other mounting approaches used in prior studies

(e.g., [5]). These boss-mounted interfaces are connected to the surrounding frames of the fuselage structure, providing a clear and direct load path for inertial forces. This architecture is also considered beneficial for crashworthiness, as it minimizes lateral mounting structures that could otherwise represent radial penetration hazards. For vacuum-insulated tank concepts, this approach can also exploit structural synergies with the existing suspension elements required to support the inner tank within the outer shell, thereby reducing the need for additional structures.

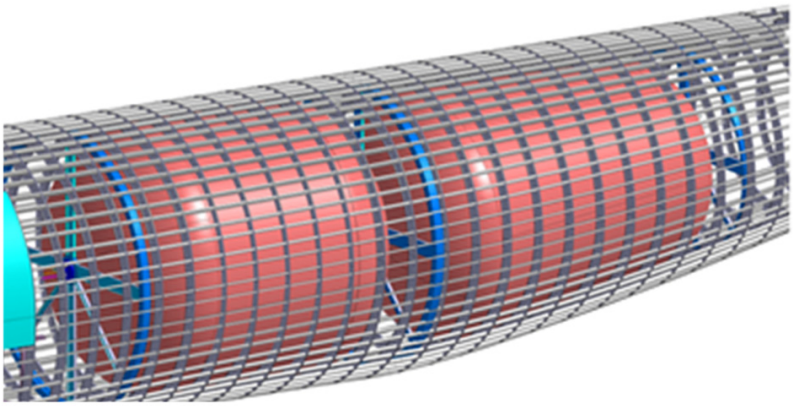

**Figure 12.** Innovative hydrogen tank integration concept featuring mounting at the tanks' bosses. This concept was mainly used for the investigations of hydrogen tanks within H2Avia.

For the structural sizing of the fuselage, *FLHYTE* bases its methodology on the NASA analytical fuselage (and wing) mass estimation approach by Ardema et al., which estimates load-bearing structural mass using fundamental structural principles at a fidelity between empirical regressions and full finite-element modeling [49]. This makes the method well suited to parametric studies, since it can be evaluated quickly while still responding to the main structural drivers, including geometry, load level, layout assumptions, and material allowables. Within *FLHYTE*, this sizing logic is applied to the modified fuselage geometry (including tank segments and/or fairings) such that the predicted structural mass responds to the altered architecture rather than implicitly assuming a conventional fuselage. In addition to the baseline fuselage constituents (skin, stringers, frames, and bulkheads), *FLHYTE* sizes the tank integration and support structures (e.g., attachments and local reinforcements) by translating mount reactions and local load introductions into sizing requirements for the attachment regions and adjacent fuselage structure.

Analogous to $LH_2$ tank modeling, calibration of hydrogen-driven mass penalties is currently limited by the lack of empirical validation data for $LH_2$ concepts of large transport aircraft. The method is therefore used primarily to compare the relative effects of different integration choices rather than to claim fully validated absolute mass values. As test, demonstrator, or industrial data become available, additional calibration inputs can be incorporated to underpin confidence in absolute mass values.

Once sizing is completed, *FLHYTE* computes the masses and CGs of the separate fuselage structural components and the tank integration structures and aggregates them into configuration-level mass properties. This component-resolved breakdown is essential for hydrogen aircraft because tank placement, fuselage elongation, and fairing installation can produce non-negligible CG shifts and structural mass penalties that must be fed back into the OAD loop for subsequent resizing and performance assessment.

#### 3.4.3. Data Exchange and Linking to the Overall Aircraft Design Loop

All output data generated by *FLHYTE* are written into standardized exchange formats to enable robust coupling to the aircraft-level design environment. In this work, results are

exported to two target formats: the aircraft exchange file used by the University Conceptual Aircraft Design and Optimization environment (*UNICADO*) and the Common Parametric Aircraft Configuration Schema (CPACS). The exported data in both files include geometric modifications, tank configuration descriptors, and mass and structural properties, such as component masses and CGs. This provides a universal data summary that can be imported by the aircraft design loop to initiate the next iteration step, both for main component sizing and for more detailed hydrogen fuel distribution system design.

For rapid plausibility checks of the resulting configuration, *FLHYTE* supports direct visualization of CPACS-based geometries using TiGL, the geometry library for processing CPACS aircraft configurations, and the associated TiGL Viewer. As shown in Figure 13, this enables the inspection of fuselage modifications, tank positioning, geometric clearances, pressure bulkhead locations, and the allocated volumes for cold boxes and related integration features immediately after the design run. The comparison also illustrates the main trade-off between both configurations: while the additional pressure bulkheads of the forward/aft tank arrangement require a longer fuselage and therefore tend to increase fuselage structural mass, the more distributed tank placement may be advantageous from an aircraft-level perspective because it can reduce CG travel during continuous defueling.

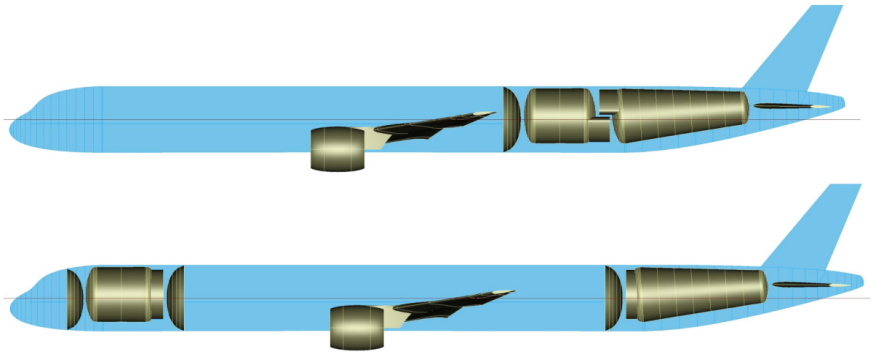

**Figure 13.** Visualizations of different SMR-H2 tank configurations in the TiGL Viewer generated with the output data of *FLHYTE*. Here, the two-aft-tank arrangement results in a fuselage length of 48.88 m, while the forward/aft tank arrangement results in 50.41 m.

#### 3.4.4. Structural Mass Effects of $LH_2$ Tank Integration

This paragraph briefly summarizes the selected fuselage design and $LH_2$ tank integration result for the SMR aircraft comparing the baseline configuration with the corresponding $LH_2$-powered variant (Figure 14). The results indicate a noticeable increase in fuselage mass for the $LH_2$ configuration, primarily resulting from the required fuselage elongation (or widening) needed to accommodate the tanks and its implications on the conventional fuselage. In addition, the explicit representation of the two $LH_2$ tank masses and the associated integration mass highlights the significantly increased structural load introduction in the wing-root region, since the fuel is no longer stored in the wing but in the fuselage. More detailed data on fuselage and tank dimensions as well as the corresponding mass values aircraft classes and variants are provided in tabulated form in the Section 4.4 of the integrated aircraft design. This is particularly important, as such quantities should be evaluated within the OAD loop to obtain converged and fully consistent results at aircraft level. Beyond the aggregated results shown here, *FLHYTE* also enables a more detailed breakdown of fuselage mass into individual airframe components, including frames, stringers, skin, bulkheads, floor structures, cut-outs, and further structural elements.

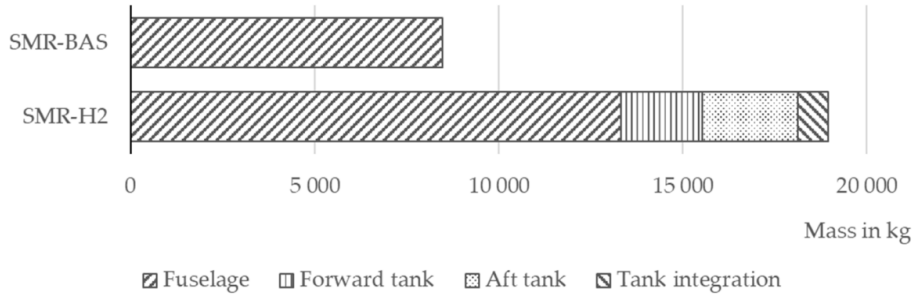


**Figure 14.** Comparison of fuselage and $LH_2$ tank masses for different SMR aircraft variants.

### *3.5. Wing*

The storage of fuel in the fuselage instead of the wing for hydrogen aircraft introduces several unconventional design opportunities as well as challenges. The absence of fuel in such "dry" wings relieves the design process from volumetric constraints, thereby allowing the possibility of developing thinner wings with significant reduction in wave drag in transonic operational regimes. On the other hand, these dry wings need to bear the entire lifting load without any alleviation from the fuel weight counteracting the lift, introducing much higher bending stresses at the wing root. Taking all these aspects into consideration, coupled aerostructural multi-disciplinary optimizations (MDOs) must be performed with the relevant technological bricks. Carbon fiber reinforced plastic (CFRP) wings have been considered in this study, which are likely to result in significant weight savings compared to their aluminum-based counterparts. This is necessary for handling the higher bending stresses, which can be foreseen in hydrogen aircraft, and is consistent with the expected technological evolution of futuristic wings.

The aerostructural design of the wings is carried out using medium fidelity methods. Euler equations with boundary layer coupling are used to evaluate the aerodynamic properties, while structural analysis is performed using linear finite element theory with a discretization based on shell elements. The aerodynamic analysis is based on the assumption of the conical 2.75D flow behavior of the wing, and the induced drag is assessed using panel methods. A Python adaptation of *conFLOW 3D* based on the work of [50] is used as the aerodynamic solver, taking into account all of the above-mentioned assumptions. The structural analysis is carried out with the structural sizing module of the preliminary aircraft design and optimization program (*PrADO*) [51–54]. The functionality of the coupled aerostructural analysis toolchain is shown in Figure 15. The optimization is carried out using the gradient-free surrogate-based Bayesian method [55]. The detailed explanation of the wing design methodology can be inferred from [56], while the discussion in this study focuses on the aerostructural performance of the resulting optimized wings.

The primary goal in the design of a wing is to identify the wing geometry in terms of its planform shape and the individual airfoil sections that minimize the drag and the structural mass of the wing. For this task, the geometry of a tapered wing with a kink and constant leading-edge sweep is assumed (see Figure 16). In the calculations, the dihedral of the wing is neglected. The profile shape at $\eta = 0.15$ shown with a terminated line is optimized and scaled to the desired thickness to chord distribution along the wingspan. Sections represented with the same color use the same profile geometry in terms of the shape and thickness to chord ratio. For the definition of the airfoil shapes, the class shape transformation geometry formulation with 14 parameters as in [50] is used.

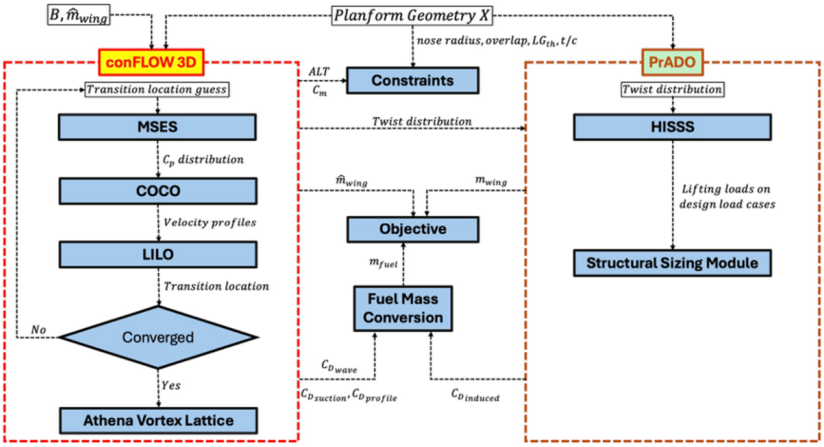


**Figure 15.** Aerostructural analysis toolchain [56].

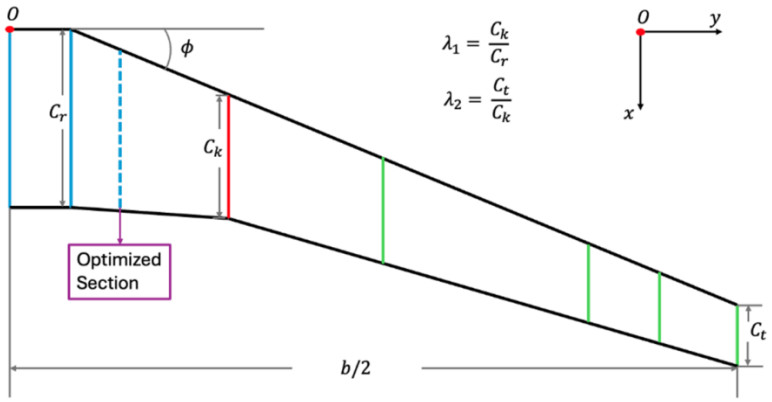


**Figure 16.** Wing geometry. The design variables are together referred as $X$ with optimized section at $\eta = 0.15$.

The number of design variables that are optimized is 20, as illustrated in Table 6. These comprise the design parameters of the airfoil profiles and planform geometry, as shown in Figure 16, together with the wing mass and parameter $B$ for the characterization of the lift distribution over the wingspan.

**Table 6.** Wing design variables.

| Design Variable | Number of Dimensions |
|---|---|
| Airfoil profile geometry | 14 |
| Leading edge sweep angle $\varphi$ | 1 |
| Taper ratios $\lambda_1$, $\lambda_2$ | 2 |
| Wingspan $b$ | 1 |
| Lift distribution parameter $B$ | 1 |
| Wing mass $m_{\text{wing}}$ | 1 |
| Total | 20 |

The lift distribution is parameterized according to Prandtl's bell shape [57], as defined in Equations (1) and (2):

$$\Theta = cos^{-1}\left(\frac{2y}{b}\right), \tag{1}$$

$$\frac{b\text{Ł}(\theta)}{L} = \frac{4}{\pi}[\sin(\theta) - B\sin(3\theta)], \tag{2}$$

The impact of $B$ on the lift distribution is illustrated in Figure 17. $B$ = 0 corresponds to an elliptic lift distribution, which is the theoretical best for minimizing the induced drag. However, it results in a heavily loaded outboard section of the wing, which increases bending stress and, consequently, the wing mass for handling them. $B$ = 1/3 corresponds to the lift distribution analytically derived by Prandtl to be the aerostructural optimal. Increasing B further results in negative lift at the tip. This negative lift is unfavorable for aircraft if not required for unconventional aspects (e.g., adverse yaw for tail-less configurations), which is out of the scope of the aircraft design space for H2Avia. Therefore, the parameter $B$ is allowed to vary between these limits of 0 and 1/3 during the aerostructural optimization of the wing.

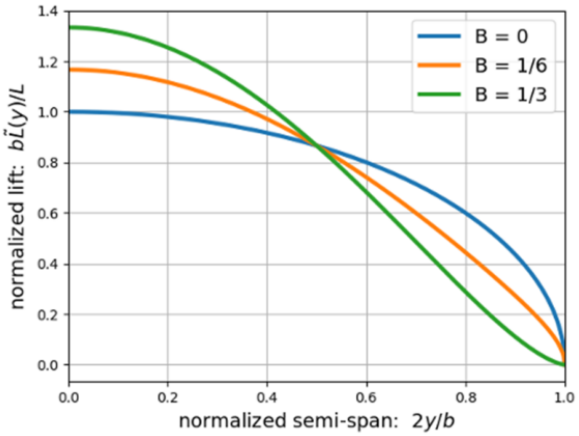


**Figure 17.** Prandtl's bell-shaped lift distribution.

The goal for the wing design is to minimize the sum of fuel mass and wing mass. The fuel mass used in this formulation is a simple approach to transform the aerodynamic objective to the same physical dimension as that of the structural objective so that the overall MDO objective constituting their summation is scientifically consistent. A constant wing area of 127 $m^2$ is ensured during the optimization. From this, the MDO problem formulation is derived as follows:

- Objective: Minimization of
  - Fuel mass + wing mass + penalty for aerostructural inconsistent wing mass.
- Design Variables:
  - Wing geometry ($X$), wing mass ($m_{\text{wing}}$), and lift distribution parameter ($B$).
- Subject to Constraints:
  - Airfoil profile thickness-to-chord ratio is greater than a prescribed threshold of 14% at the design section;
  - No negative volume/overlapping profile shape;
  - Nose radius of the airfoil is greater than the prescribed threshold of 8 mm;
  - Moment coefficient $C_m$ is greater than the prescribed threshold of $-0.15$;
  - Minimum thickness to accommodate the landing gear.

The resultant optimized wing from the MDO possessed an aspect ratio of 9.5, and the lift distribution parameter $B$ = 0.084 for a cruising $C_L = 0.58$. It is assumed that the entire lift is being generated by the wing, with no lift contribution from the empennage. However, during the OAD, it is advantageous to also consider the sensitivity of the entire aircraft, e.g., the aspect ratio. Hence, additional sensitivity studies were conducted on the optimized wing configuration for these parameters, as illustrated in Figure 18.

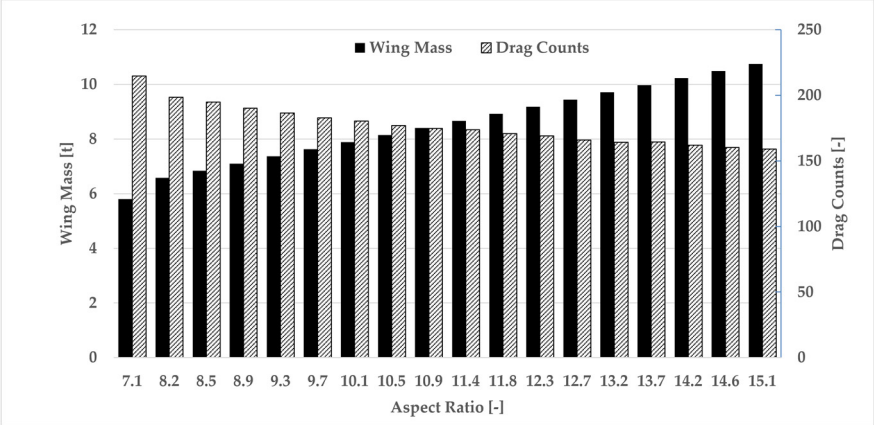


**Figure 18.** Aspect ratio sensitivity for the SMR-BAS with a wing area of 127 $m^2$.

The data in Figure 18 were integrated into the SMR-BAS OAD, thereby enabling the identification of the optimal selection of aspect ratio for the assessment on overall aircraft level. The OAD aerodynamic methods for the wing were calibrated to the MDO results for different aspect ratios (see Figure 18). At the OAD level, the best performance in terms of block energy was achieved with an aspect ratio of 13.2. Changes in the wing area during the OAD design loop, caused by a fixed wing loading, were translated to the wings' aerodynamic performance by using the calibrated OAD methods (see Section 4.3.4). The characteristics of the resulting wing configuration of the SMR-BAS wing are given and compared against those for SMR-REF wing in Table 7. It is evident that the SMR-BAS wing exhibits significantly lower wave drag. A better L/D ratio is obtained by the SMR-BAS wing. The impact of using CFRPs in the wing design is also evident, where a significant increase in the aspect ratio has been achieved, without any weight penalties in comparison to the aluminum-based SMR-REF wing. In fact, the SMR-BAS wing is still 4% lighter despite having a 31% higher aspect ratio. The SMR-BAS wing design also serves as the main reference for extrapolating to the corresponding wing characteristics for the SMR-H2.

**Table 7.** Comparison of wing characteristics for the optimized SMR-BAS wing vs. SMR-REF wing.

| Parameter | SMR-REF | SMR-BAS (OAD) |
|---|---|---|
| Lift coefficient | 0.58 | 0.58 |
| Aspect ratio | 10.1 | 13.2 |
| Sweep angle [deg] | 27.0 | 28.2 |
| Wing area [$m^2$] | 127 | 119 |
| Wing mass [kg] | 9399 | 9027 |
| Span [m] | 35.8 | 39.7 |
| Wave drag | 0.0023 | 0.0002 |
| Viscous drag | 0.0069 | 0.0067 |
| Induced drag | 0.0131 | 0.0105 |
| Total wing drag | 0.0223 | 0.0174 |
| Wing L/D | 26.0 | 33.3 |

Consequently, the REG-BAS wing design is also scaled from the SMR-BAS, since it was designed for the same Mach number. Since the LR-REF aircraft, inspired from the Airbus A350, is already equipped with a CFRP wing, an aerostructural redesign was not carried out, and the reference wing was utilized for all the long-range aircraft designs.

## 4. Integrated Aircraft Design

This section describes the integration of the hydrogen technologies presented in the previous sections into the OAD environment *UNICADO* [27]. The integrated aircraft design serves the purpose of calculating detailed aircraft properties for all three size classes (REG, SMR, and LR) and all three technology levels (REF, BAS, and H2), thereby providing consistent input for the holistic assessment described in Section 5.

### *4.1. Top-Level Aircraft Requirements*

The top-level aircraft requirements (TLARs) of the individual aircraft sizes are shown in Table 8 gathered from public sources [58–60]. These requirements remain constant for all application cases (i.e., REF, BAS, and H2) to ensure a fair and consistent comparison.

**Table 8.** TLARs of the different aircraft sizes.

| Requirement | Unit | REG | SMR | LR |
|---|---|---|---|---|
| Design/study payload | kg | 11,400 | 17,100 | 30,875 |
| Maximum payload | kg | 15,128 | 19,300 | 53,400 |
| Design passengers | - | 120 | 180 | 325 |
| Design range | NM | 2940 | 2943 | 8100 |
| Study range | NM | 800 | 800 | 4000 |
| Cruise Mach number | Ma | 0.78 | 0.78 | 0.85 |
| Maximum take-off field length | m | 1873 | 1951 | 2588 |
| Maximum landing field length | m | 1720 | 1880 | 1960 |
| Maximum approach speed | kts | 132 | 138 | 140 |
| Maximum operating altitude | ft | 38,500 | 40,000 | 43,100 |
| Maximum Mach number | Ma | 0.82 | 0.82 | 0.89 |

### *4.2. Technology Assumptions*

The reference aircraft (X-REF) form the starting point for the baseline (X-BAS) and hydrogen (X-H2) aircraft, to which evolutionary technologies likely for an EIS in 2040 are applied. These technological improvements comprise ultra-high bypass ratio geared turbofan engines (see Table 3) and a more electric systems architecture. The latter implies the elimination of the pneumatic system and, accordingly, electric de-icing and an electric environmental control system (ECS). It was additionally assumed that the fuselage and wings are manufactured from CFRPs and are covered with riblets [61]. Furthermore, mass reduction factors were applied, as shown in Table 9.

**Table 9.** Technology factors assumed for EIS 2040 applied to X-BAS and X-H2 [62].

| Parameter | Value |
|---|---|
| Relative fuselage and wing viscous drag reduction due to riblets | 4.0% |
| Relative empennage mass reduction | 5.0% |
| Relative landing gear mass reduction | 5.0% |
| Relative dry wing mass increase | 4.8% |

The dry wing mass increase of 4.8% accounts for the heavier structural masses required to compensate for the loss of bending moment relief when shifting the fuel from the wing to the fuselage, as is standard practice for hydrogen-powered aircraft. This value was determined based on a comparative assessment of the semi-empirical and semi-analytical wing mass estimation methods of Niu [63], Torenbeek [64], and Jenkinson [65]. The method of Torenbeek [64] was finally selected to predict an average value for the three hydrogen-powered aircraft analyzed in this paper, as this method showed the best agreement with

the high-fidelity results from the aerostructural optimization (see Section 3.5) and is further supported by recent findings for an A321-class aircraft [66].

### *4.3. Integration Strategy*

The design of the reference aircraft follows well-established procedures for redesigning existing aircraft in *UNICADO*. In contrast, the design of the baseline (X-BAS) and hydrogen (X-H2) aircraft for an EIS in 2040 requires new approaches for the integration of partner contributions [27,28]. A dedicated synthesis strategy for the H2Avia baseline and hydrogen aircraft was developed [3] and is shown in Figure 19.

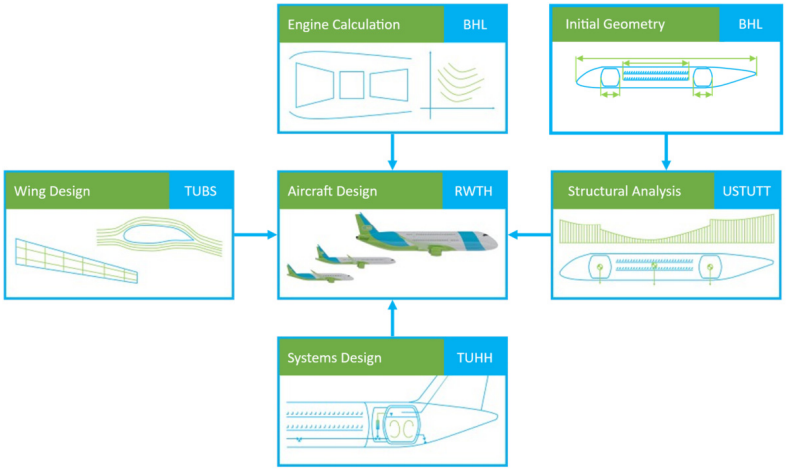


**Figure 19.** Synthesis strategy for the H2Avia hydrogen aircraft [3].

To integrate the various models of the subdisciplines described in the previous sections, interfaces were defined that enable data exchange. The CPACS file format serves as the central exchange format at the overall aircraft level [40]. At the module level, the modeling already available in *UNICADO* was replaced by the higher-fidelity models of the partners for propulsion, system architecture, fuselage and wing design, as well as hydrogen tank integration.

#### 4.3.1. Propulsion

For the engine model integration, engine decks were created for each engine, listing the thrust and fuel consumption as a function of Mach number, flight altitude, and power setting. During take-off and climb, the maximum available thrust for the given altitude and Mach number is used, and the corresponding fuel consumption is multiplied by the duration of each flight interval to calculate the accumulated fuel burn. During cruise, the thrust is set equal to drag, from which the required engine setting (in terms of N1) and the respective fuel consumption are determined. $NO_x$ emissions are calculated analogously based on the emission indices described in Table 3. The engines were designed by Bauhaus Luftfahrt at the ToC operating point for each configuration (see Table 3), resulting in a fixed engine geometry and a fixed sea-level static thrust for each variant. In the *UNICADO* aircraft design process, the engines were integrated as off-the-shelf components without further resizing. Consequently, the thrust-to-weight ratio at take-off is not a design input but a result of the aircraft-level convergence, reflecting the interaction between the fixed engine thrust and the converged maximum take-off mass (MTOM) for each configuration.

#### 4.3.2. Systems

The integration of on-board systems into the OAD encompasses both conventional and hydrogen-specific systems. For the reference aircraft (X-REF), the on-board systems

were sized using the *UNICADO* systems module, which employs established empirical mass and power estimation methods.

To improve the fidelity of the systems representation for the baseline and hydrogen aircraft, the *UNICADO* systems results for the SMR-REF were calibrated against the higher-fidelity results obtained from the *GeneSys* framework at the Hamburg University of Technology (see Section 3.3). Scaling factors were derived for all major on-board systems by comparing the *UNICADO* estimates to the *GeneSys* sizing results at the SMR level. Particular attention was paid to three systems that undergo fundamental changes in the transition to BAS and H2 configurations:

Fuel system: For the baseline aircraft, the conventional kerosene fuel system is retained. For the hydrogen variants, the kerosene fuel system is entirely replaced by the $LH_2$ supply system sized by *GeneSys* (see Table 5), including cold boxes, distribution pipes, venting lines, and associated power consumers.

ECS: For the BAS and H2 configurations, the ECS is operated electrically (bleedless), replacing the conventional pneumatic supply from the engines. This results in a modified power off-take profile and an increase in electrical system mass, which was captured through the calibrated scaling factors.

Ice protection system: Analogously, the anti-ice system transitions from a pneumatic bleed-air-based architecture to an electro-thermal system for both BAS and H2 aircraft, consistent with the bleedless engine architecture.

The scaling factors derived for the SMR were subsequently applied to the REG and LR aircraft as well, ensuring a consistent systems representation across all size classes. The cold box geometry was integrated within *FLHYTE* as part of the fuselage geometry calculation.

#### 4.3.3. Fuselage

The cabin and fuselage design process starts from the cabin layouts defined by Bauhaus Luftfahrt using the tools *CAFE* and *HyDRA* (see Section 3.4), which are provided to both *FLHYTE* and *UNICADO* via the CPACS interface. The fuselage and tank integration was performed using the tool *FLHYTE*, developed by the University of Stuttgart (see Section 3). *FLHYTE* was designed to integrate directly into the *UNICADO* workflow, communicating with the *UNICADO* aircraft exchange file without intermediate manual data transfer. Within the aircraft design convergence loop, *FLHYTE* receives the outer fuselage geometry and the required fuel volume from the *UNICADO* sizing modules as primary inputs.

For the hydrogen aircraft (X-H2), the user specifies the tank layout (number and placement of tanks) via the module configuration file. Based on this layout and the available fuselage envelope, *FLHYTE* calculates the space-optimized $LH_2$ tank structure, including the integrated cold box and crashworthiness structure, as well as the corresponding tank mass and center of gravity (see Section 3). The updated geometric and mass properties are then written back to the aircraft exchange file, triggering the next steps of the *UNICADO* convergence loop.

For the baseline aircraft (X-BAS), which store SAFs in conventional wing tanks, no hydrogen tank integration is required. In this case, *FLHYTE* calculates the fuselage structural mass for the given cabin layout using the same semi-analytical methodology (see Section 3), thereby ensuring a consistent fuselage mass estimation approach across all technology levels.

#### 4.3.4. Wing

The integration of the wing design follows a combined approach using the high-fidelity aerostructural results from TU Braunschweig (see Section 3.5) to calibrate the lower-fidelity wing models employed in *UNICADO*.

The aerostructural aspect ratio sensitivity study presented in Section 3 was conducted at two levels of fidelity: (i) a high-fidelity coupled aerostructural optimization using *conFLOW 3D* and *PrADO* and (ii) a corresponding study within *UNICADO*. From the comparison, scaling factors for wing mass and drag were derived to ensure that the effects of the optimized wing geometry are correctly represented in *UNICADO*. The criterion for aspect ratio selection was the minimization of block energy, since the primary objective of the H2Avia assessment is to evaluate the energy efficiency of hydrogen aircraft. For the SMR-BAS and SMR-H2 aircraft, an aspect ratio of 13.2 was selected, as this value yielded the minimum block energy in the combined aerostructural study (see Figure 18). Notably, the optimization demonstrates that the combination of CFRP wing material and optimized transonic airfoils enables the higher aspect ratio without a wing mass penalty: the SMR-BAS wing mass is 9027 kg compared to 9399 kg for the SMR-REF (−4%), while the wing L/D improves from 32.4 to 36.4 (+12%). This improvement is primarily driven by a 69% reduction in wave drag through the optimized airfoils.

For the LR-BAS and LR-H2 aircraft, an aspect ratio of 13.2 was likewise adopted. Since the Airbus A350 reference aircraft already features a CFRP wing, no dedicated aerostructural redesign was conducted for the LR class. Instead, the reference wing was scaled to the target aspect ratio using the technology factors from Table 9 and the scaling relationships derived from the SMR study.

For both classes (SMR and LR), the resulting wingspans (39–41 m and 72–76 m, respectively) exceed the gate category of the corresponding reference aircraft, representing a transition from Code C to Code D for the SMR and from Code E to Code F for the LR. This was accepted in view of the demonstrated energy benefit and the projected EIS of 2040 (e.g., using foldable wingtips). For the REG aircraft, it was a deliberate project decision to retain the aspect ratio of the Airbus A220 reference, considering the much younger design and therefore advanced technology level. This resulted in a maximum aspect ratio of approximately 11.0 for both REG-BAS and REG-H2.

The wing design methodology and scaling factors derived from the SMR aerostructural study (see Section 3.5) were applied accordingly to the REG and LR aircraft, yielding the wing planform geometry for each baseline configuration. After convergence of the MTOM, a wing loading resulted for each baseline aircraft. For the comparison between baseline and hydrogen variants—which is the focus of the technological assessment in H2Avia—the wing loading was kept constant within each aircraft class, as the wing was not redesigned but only resized to accommodate the changed MTOM. Consequently, the wing area scales with the MTOM at constant wing loading for BAS and H2 of each class. Aerodynamic polars for all flight phases were calculated based on the resulting wing geometry and aircraft shape using the low-fidelity models from *UNICADO* corrected to the high-fidelity sensitivities of the SMR-BAS study (see Section 3). The wing mass for the hydrogen variants additionally accounts for the dry wing penalty factor of 4.8% (see Table 9).

### *4.4. Aircraft Performance*

The results of the integrated baseline and hydrogen preliminary aircraft designs allow for a fair comparison of the aircraft's performance. In the following, the results are presented in tables and figures and then discussed in more detail. The key parameters of the aircraft are presented in Table 10.

A detailed breakdown of the hydrogen tank and system parameters is provided in Table 11.

A visualization of the geometry, including hydrogen tanks and cold boxes, can be found in Figures 20–22.

**Table 10.** Comparison of the key aircraft parameters for all three aircraft classes (REG, SMR, and LR) with kerosene (BAS) and hydrogen (H2) as fuel.

| Parameter | Unit | REG-BAS | REG-H2 | SMR-BAS | SMR-H2 | LR-BAS | LR-H2 |
|---|---|---|---|---|---|---|---|
| Cabin seating | - | 2-3 | 3-3 | 3-3 | 2-3-2 | 3-3-3 | 2× 3-4-3 |
| Fuselage width | m | 3.51 | 3.95 | 3.95 | 4.96 | 5.96 | 7.14 |
| Fuselage height | m | 3.72 | 4.14 | 4.14 | 4.56 | 6.09 | 8.75 |
| Fuselage length | m | 35.0 | 43.24 | 37.57 | 48.88 | 65.27 | 69.61 |
| Span | m | 33.87 | 35.29 | 39.65 | 41.09 | 76.4 | 72.46 |
| Wing area | $m^2$ | 104 | 113 | 119 | 128 | 449 | 404 |
| Aircraft $L/D_{cruise}$ | - | 19.2 | 18.6 | 21.3 | 18.8 | 22.6 | 20.4 |
| Δ rel. | - | −3% | | −12% | | −10% | |
| Wing mass | kg | 5810 | 6593 | 9027 | 9771 | 37,385 | 29,486 |
| Fuselage mass | kg | 6662 | 9550 | 8468 | 13,328 | 26,971 | 36,456 |
| Propulsion group mass | kg | 7533 | 8309 | 7750 | 8507 | 16,736 | 17,097 |
| Operating mass empty | kg | 33,863 | 45,338 | 43,038 | 56,464 | 129,287 | 158,081 |
| MTOM | kg | 56,423 | 61,260 | 74,105 | 79,526 | 247,344 | 222,598 |
| Δ rel. | - | +9% | | +7% | | −10% | |
| Block energy design mission | GJ | 410 | 464 | 522 | 616 | 3229 | 3492 |
| Δ rel. | - | +13% | | +18% | | +8% | |
| Block energy study mission | GJ | 121 | 143 | 157 | 188 | 1468 | 1697 |
| Δ rel. | - | +18% | | +20% | | +16% | |

**Table 11.** Comparison of hydrogen tank and system parameters.

| Parameter | Unit | REG-H2 | SMR-H2 | LR-H2 |
|---|---|---|---|---|
| Tank diameter | m | 3.5 | 3.9 | 6.9 |
| Forward tank length | m | 3.7 | 4.8 | 7.2 |
| Aft tank length | m | 9.4 | 6.4 | 10.7 |
| Forward tank volume | $m^3$ | 25.9 | 44.7 | 216.7 |
| Aft tank volume | $m^3$ | 44.5 | 48.1 | 306.5 |
| Forward tank mass | kg | 1854 | 2965 | 11,953 |
| Aft tank mass | kg | 3722 | 3507 | 16,979 |
| Forward tank hydrogen mass | kg | 1735 | 2990 | 14,508 |
| Aft tank hydrogen mass | kg | 2980 | 3224 | 20,519 |
| Forward tank GI | - | 48% | 50% | 55% |
| Aft tank GI | - | 44% | 48% | 55% |
| Cold box mass | kg | 542 | 554 | 576 |
| Pipe and venting mass | kg | 658 | 747 | 907 |

#### 4.4.1. Fuselage and Seating Layout

The transition from kerosene to hydrogen has a significant impact on the fuselage design. The integration of $LH_2$ tanks in the fuselage necessitates an increase in the fuselage cross-section to ensure a favorable tank surface-to-volume ratio and adequate space for landing gear integration while maintaining an acceptable fuselage slenderness ratio. For each aircraft class, a seating layout was selected that is appropriate for the resulting fuselage diameter: the REG-H2 adopts a 3-3 layout (widened from 2-3) to accommodate a fuselage width of 3.95 m, the SMR-H2 transitions to a 2-3-2 twin-aisle arrangement at 4.96 m width, and the LR-H2 features a double-deck 3-4-3 configuration at 7.14 m width. The double-deck design for the LR was necessary to maintain a reasonable slenderness ratio, as a single-deck configuration would have resulted in an excessively long fuselage. The wider cross-section also offers the advantage of shorter, more volumetrically efficient hydrogen tanks (see Section 3.4).

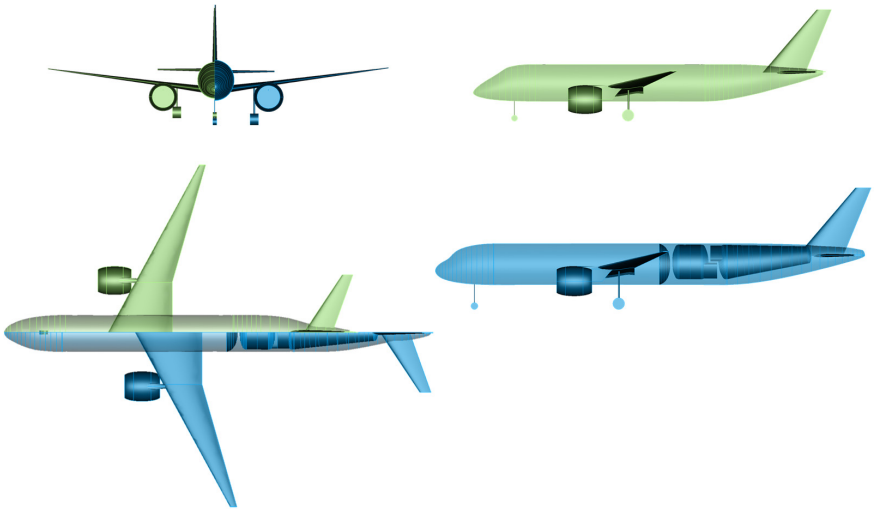

**Figure 20.** Three-sided view of REG-BAS (green) and REG-H2 (blue) in the TiGL Viewer.

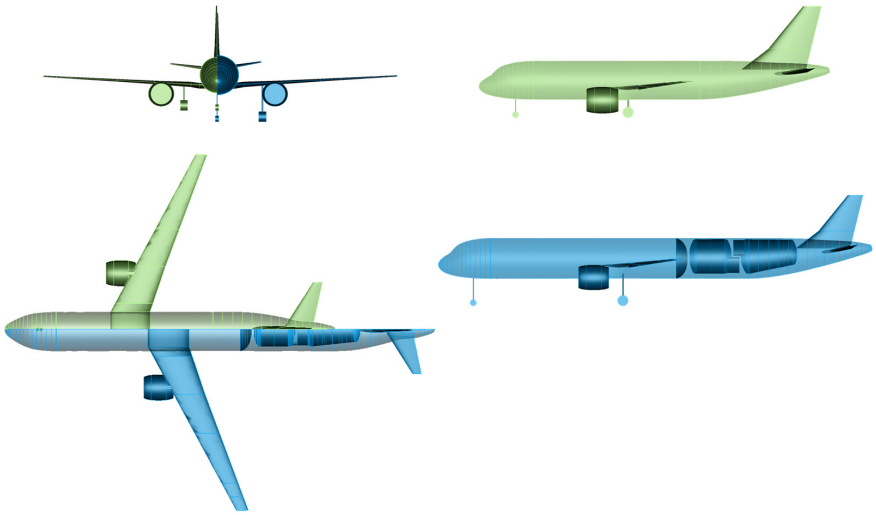

**Figure 21.** Three-sided view of SMR-BAS (green) and SMR-H2 (blue) in the TiGL Viewer.

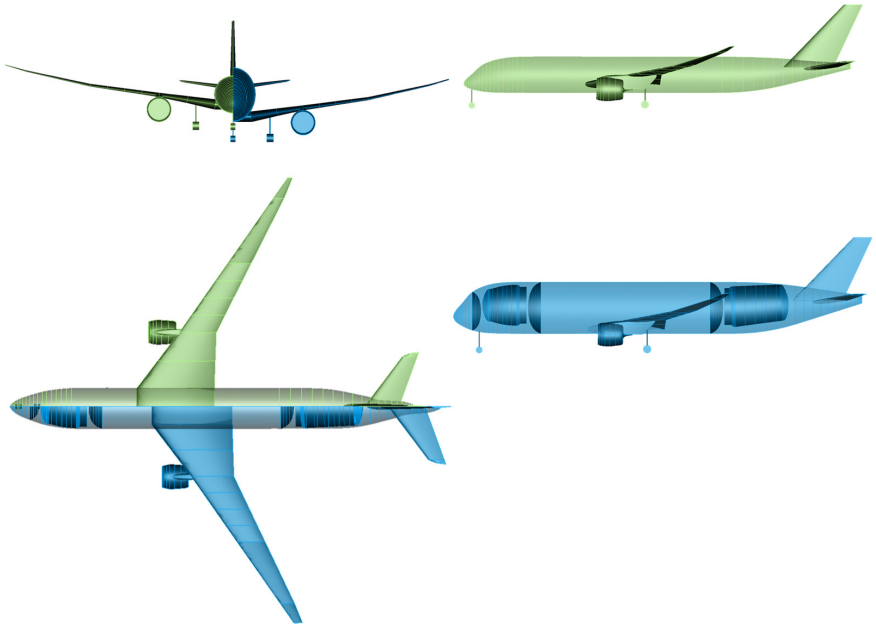

**Figure 22.** Three-sided view of LR-BAS (green) and LR-H2 (blue) in the TiGL Viewer.

#### 4.4.2. Gravimetric Index

The tank GI ranges from 44% (REG-H2 aft tank) to 55% (LR-H2 both tanks). The trend of increasing GI with tank diameter is to be expected and consistent with the literature. Huete and Pilidis [7] demonstrate that gravimetric efficiency increases substantially with tank diameter, ranging from approximately 10% for very small tanks (0.5 m) to nearly 80% for very large tanks. The FlyZero study project's GI of 47% (REG)–58% (LR) for a first-generation EIS and 64–75% for a 2050 technology level [67]. The values in Table 11 for the 2040 timeframe are positioned within this expected range. The higher GI for the LR tanks is directly attributable to the larger tank diameter (6.9 m vs. 3.45–3.87 m), which improves the surface-to-volume ratio and thereby reduces the relative contributions of insulation mass and structural mass. Additionally, the forward tanks consistently exhibit a slightly higher GI than the aft tanks of the same aircraft, as their geometry tends to be more spherical (shorter length at similar diameter).

#### 4.4.3. Aerodynamic Performance

The cruise lift-to-drag ratio (L/D) decreases for all hydrogen aircraft compared to their baselines: from 19.2 to 18.6 (−3%) for the REG, from 21.3 to 18.8 (−12%) for the SMR, and from 22.6 to 20.4 (−10%) for the LR. The L/D degradation is driven by the increased fuselage dimensions required for tank integration, which affect both friction drag (through increased wetted area) and pressure drag (through the larger cross-section). The SMR-H2 exhibits the largest relative L/D reduction, as the fuselage width increases by 26% (from 3.95 m to 4.96 m) and the fuselage length by 30% (from 37.57 m to 48.88 m) due to the transition from a single-aisle to a twin-aisle cross-section. For the LR-H2, the double-deck configuration partially mitigates this effect: while the fuselage width increases by 20% (from 5.96 m to 7.14 m), the fuselage length increases by only 7% (from 65.27 m to 69.61 m), as the wider cross-section accommodates the hydrogen tanks in a more spherical arrangement. The REG-H2 shows the smallest L/D penalty (−3%), as the fuselage width increase is moderate (+13%, from 3.51 m to 3.95 m), although the fuselage length increases by 24% (from 35.0 m to 43.24 m).

#### 4.4.4. Mass Properties

The operating mass empty (OME) increases significantly for all hydrogen variants: by +34% for the REG-H2 (45,338 kg vs. 33,863 kg), +31% for the SMR-H2 (56,464 kg vs. 43,038 kg), and +22% for the LR-H2 (158,081 kg vs. 129,287 kg). The primary contributors to this increase are the heavier fuselage structure (due to elongation, widening, and local reinforcement at the tank interfaces), the hydrogen tank and system mass (including tanks, cold boxes, distribution pipes, and venting lines; see Table 11), and the dry wing mass penalty of 4.8% from the absence of fuel-based bending moment relief. The relatively lower OME increase for the LR-H2 is attributable to the smaller wing area (404 $m^2$ vs. 449 $m^2$), which reduces the wing mass from 37,385 kg to 29,486 kg (−21%), partially offsetting the fuselage mass increase from 26,971 kg to 36,456 kg.

The resulting MTOM changes range from +9% (REG-H2) and +7% (SMR-H2) to −10% (LR-H2). The substantially lower MTOM changes compared to the OME increases are explained by the reduced fuel mass: hydrogen's 2.8 times higher gravimetric energy density results in significantly lighter fuel loads, which largely compensate for the structural overhead. For the LR-H2, the fuel mass saving at the 8100 nm design range, combined with the reduced wing area, more than offsets the OME increase, resulting in a net MTOM reduction of 10% despite the +22% higher OME. These trends are consistent with the Cryoplane study [6], which reported MTOM changes between +4.4% for small regional aircraft and −14.8% for long-range aircraft, confirming that the MTOM balance becomes

increasingly favorable with aircraft size and design range as the fuel mass saving from hydrogen's higher gravimetric energy density grows relative to the structural overhead. Similarly, Onorato et al. find a 4% MTOM reduction for a comparable configuration [8]. The SMR-H2 in H2Avia shows a less favorable MTOM outcome (+7%) compared to these references. This is primarily attributed to the substantial fuselage cross-section enlargement from 3.95 m to 4.96 m (single aisle to twin aisle), which represents the most significant geometric change among the three H2Avia aircraft classes and leads to both the highest L/D degradation (−12%) and the largest fuselage mass increase. This suggests that the SMR-H2 configuration may have further optimization potential, for instance, through alternative cabin cross-sections or fuselage geometries that reduce the aerodynamic and structural penalties of tank integration.

#### 4.4.5. Energy Consumption

The hydrogen aircraft require 8–20% more block energy than the corresponding baselines, depending on aircraft class and mission range. On the design mission, the increase is +13% (REG), +18% (SMR), and +8% (LR). The SMR energy delta, although being the largest, is still in the range of results reported in the literature (e.g., 23%; see [66]). On the shorter study missions, the penalties are higher: +18% (REG), +20% (SMR), and +16% (LR). A direct comparison of absolute values with other studies is of limited significance, as the energy penalty depends strongly on the specific design assumptions, including design range, GI, tank configuration, and fuselage cross-section. However, the trends observed in H2Avia are consistent with the literature: the energy penalty is lowest for the long-range aircraft, where hydrogen's higher gravimetric energy density provides the greatest cumulative fuel mass saving, and increases for shorter missions, where the fixed structural mass overhead becomes proportionally more significant. This range-dependent trend is corroborated by findings from the Cryoplane project, which showed that long-distance flights can benefit from hydrogen propulsion while short-haul flights incur energy penalties.

### *4.5. Mission Trajectories*

The design mission trajectory for the LR-BAS and LR-H2 is shown in Figure 23. A characteristic difference between baseline and hydrogen aircraft is the flatter decrease in the lift coefficient during cruise at constant flight level. This is because hydrogen has approximately 2.8 times higher gravimetric energy density than kerosene, resulting in a lower fuel mass for the same energy content. Consequently, the aircraft mass and, thus, the required lift decrease less steeply during cruise for the hydrogen aircraft, which, in turn, leads to fewer step climbs. These effects occurred for all aircraft sizes.

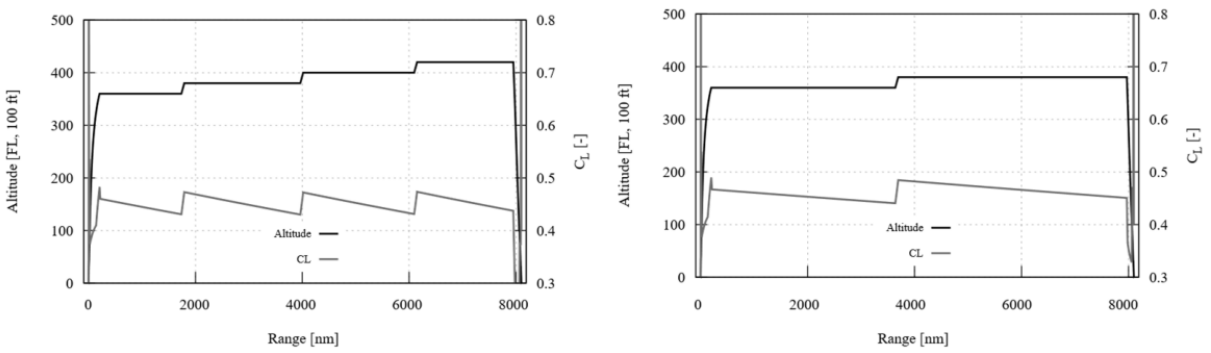


**Figure 23.** Mission trajectory of LR-BAS (**left**) and LR-H2 (**right**) for the design mission.

### *4.6. Payload Range*

An overview of the payload range characteristics of the three aircraft classes is given in Figure 24. Since the TLARs define the same design point (design payload and design range) for both baseline and hydrogen aircraft of each class (see Table 8), the boundary lines of their respective payload range diagrams intersect at this point on the MTOM line. Despite identical TLARs, the payload range envelopes of hydrogen and kerosene aircraft differ significantly in three characteristic ways:

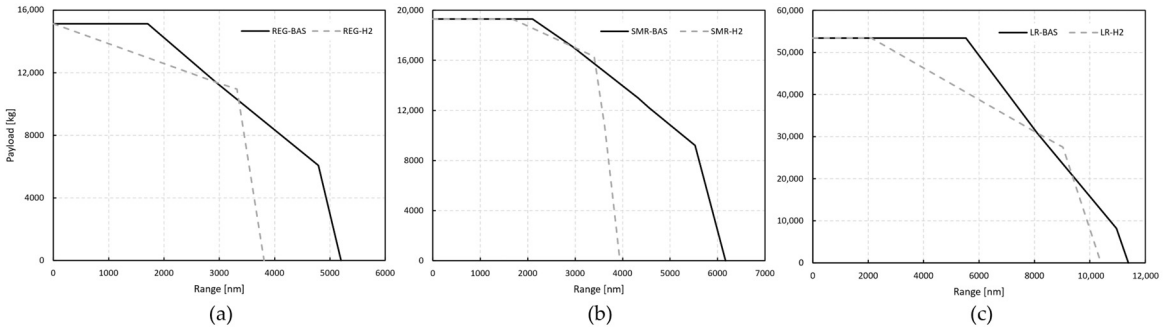


**Figure 24.** Payload range diagram of BAS and H2 for (**a**) REG, (**b**) SMR, and (**c**) LR.

First inflection point (maximum range at maximum payload): For the hydrogen aircraft, the OME at maximum payload is closer to the MTOM due to the higher structural mass (heavier fuselage, tanks, and dry wing). This means that the available mass budget for fuel at maximum payload is smaller, and consequently, the maximum range at maximum payload is significantly shorter than for the baselines.

Slope between inflection points: Beyond the first inflection point, the boundary line for hydrogen aircraft runs more flatly (i.e., range increases more for a given payload reduction) than for the baseline. This is because hydrogen carries more energy per unit mass, so trading one kilogram of payload for one kilogram of additional fuel yields a greater range increment.

Second inflection point (maximum tank capacity): The hydrogen tanks have a finite maximum capacity that is 3.5% above the capacity for the design point [8]. To fly beyond this range with a hydrogen aircraft, larger and heavier tanks would be required, which would impose weight and drag penalties at shorter ranges. In contrast, kerosene aircraft benefit from the large fuel storage volume available in the wing, resulting in a significantly higher maximum range at MTOM. Beyond the second inflection point, where maximum tank capacity is reached, only payload is reduced. In this region, the boundary lines for kerosene and hydrogen aircraft run approximately parallel in each class, as the maximum range is predominantly limited by aerodynamic efficiency and engine performance rather than the type of fuel.

These characteristics have direct implications for airline operations: hydrogen aircraft are best suited for missions at or near their design range, where the efficiency and payload capability are optimized. For missions significantly shorter than the design range, the fixed structural mass overhead of the hydrogen tanks leads to a disproportionate efficiency penalty, while for missions significantly longer, the limited tank capacity restricts the operational envelope.

## 5. Holistic Assessment

### *5.1. Climate Assessment from Aircraft Operations*

This section assesses the climate impact from aircraft operations for the investigated aircraft concepts, accounting for both $CO_2$ emissions and non-$CO_2$ effects during flight.

Fleet-level climate impacts are computed with an in-house climate-impulse response model, which provides key performance indicators including emissions, radiative forcing (RF), and global mean surface temperature change (ΔT). The model follows the linear impulse-response framework proposed by Sausen et al. [68] and further developed by Grewe et al. [69] and Dallara et al. [70], assuming the climate system responds approximately linearly to small perturbations around a quasi-stationary background state. Time integration of the response functions yields integrated climate metrics (e.g., average temperature response (ATR, GWP)). The efficacy-weighted global warming potential ($f$-$GWP_{100}$) metric was selected as the primary metric as it incorporates climate efficacies, yielding relative forcing contributions consistent with temperature-based metrics such as ATR.

The climate model is coupled to the fleet model to capture differences across aircraft types and regional operations. For each aircraft concept (REG, SMR, and LR; reference, baseline, and $H_2$), an emission profile is generated using emission indices for kerosene and hydrogen. The model evaluates representative missions for each aircraft–region combination and computes climate metrics for each emitted species and corresponding impact. To illustrate the results, Figure 25 shows the relative contribution of each forcer/emission to the total $f$-$GWP_{100}$ metric for a typical mission.

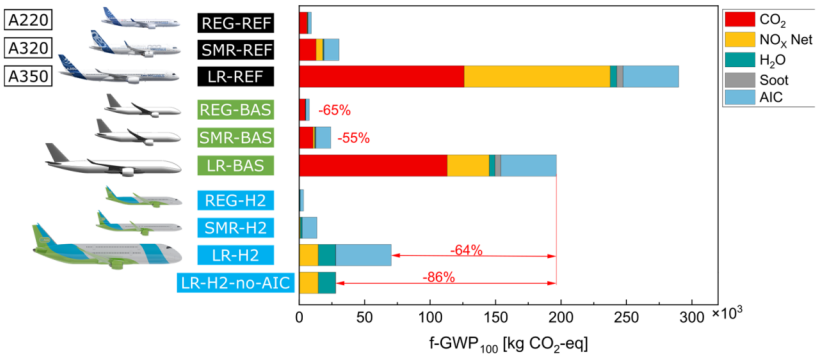


**Figure 25.** Comparison of climate impact using the efficacy-weighted GWP100 metric. Climate impact reductions are shown relative to the corresponding baseline aircraft for representative route-pair missions: North America short haul, 518 km; Asia medium haul, 1574 km; and Europe–North America long haul, 6730 km.

AIC, including contrail cirrus, constitutes the dominant source of uncertainty in the climate impact assessment [71,72]. This uncertainty is particularly relevant for $LH_2$ aircraft, as the interaction between the water vapor emissions and volatile and non-volatile particulate matter on contrail properties remains [73–75]. To address this uncertainty in a transparent way, two scenarios for the $LH_2$ AIC contribution were considered: (i) a low-impact case in which AIC impacts are strongly mitigated by operational measures and reduced contrail lifetime (see Figure 25, LR-H2 and LR-H2-no-AIC) and (ii) a high-impact case in which increased $H_2O$ emissions lead to AIC effects comparable to those of a kerosene aircraft. Together, these two scenarios define the bounds within which the AIC contribution of $LH_2$ operations is accounted for in the present analysis.

Figure 25 (yellow bar) shows the contribution associated with $NO_x$ emissions, accounting for the coupled effects on atmospheric $CH_4$ and $O_3$: $CH_4$ reduction and the associated long-term decrease in $O_3$ (negative RF), as well as the short-term increase in $O_3$ (positive RF). The model considers the altitude dependence of these effects through average forcing factors, parameterized as a function of cruise altitude and mission duration [70,76]. This altitude sensitivity is reflected in the varying relative $NO_x$ contribution across aircraft sizes observed in Figure 25, since aircraft size influences the typical cruise altitude and therefore the magnitude of the $NO_x$-related climate impact.

### *5.2. Life-Cycle Assessment*

The LCA model builds on the production assessment and includes a detailed representation of the green hydrogen supply chain, covering $GH_2$ production via electrolysis, hydrogen liquefaction, and subsequent transport. Figure 26 presents the emission breakdown for the production and transport of $LH_2$ for a wind-based scenario from Lettercamps to FRA (Figure 26a) and for the solar-based scenario from Ouarzazate to FRA (Figure 26b). In both scenarios, emissions are primarily driven by the production of $GH_2$, largely due to the high electricity demand of water electrolysis. The second most impactful contributor is the liquefaction of hydrogen. Operating the liquefaction plant at an economic optimum requires different battery storage sizes to buffer fluctuations in renewable electricity supply. In the wind-based scenario, extended periods of low electricity generation necessities a larger battery capacity. This increases the relative emission share associated with battery production and operation, thereby raising the overall contribution of the liquefaction stage. In the solar-based scenario, additional inland transport of $LH_2$ from the production facility to the harbor introduces an additional emission source. These emissions are substantially higher than those associated with maritime transport.

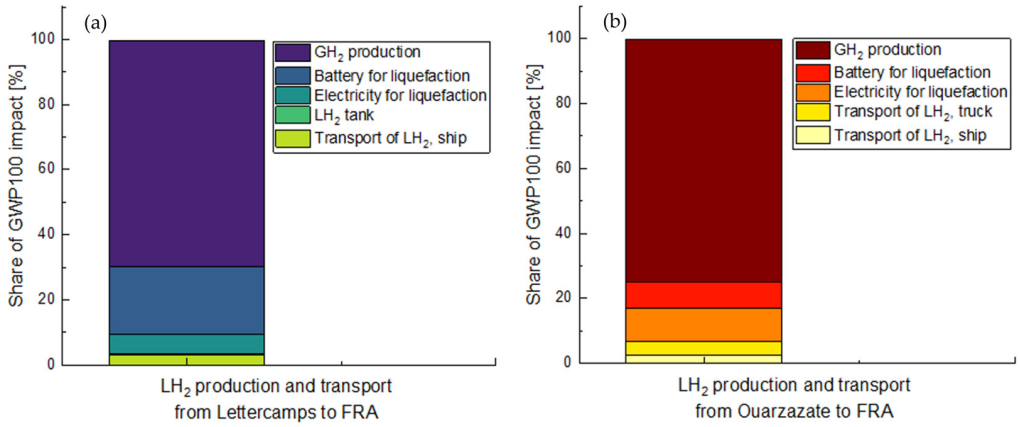


**Figure 26.** Share of the GWP100 contribution (%) from production in Ireland (**a**) and Morocco (**b**) to the transport to Frankfurt Airport.

### *5.3. Global Fleet Assessment*

The global fleet assessment within H2Avia evaluates the potential of hydrogen-powered aircraft at the fleet level using a scenario-based, optimization-driven fleet modeling framework. The aim is to simulate how different aircraft technologies, operational measures, and fuel regulations influence global fleet composition, energy consumption, and climate impact over time. The assessment follows a top-down approach [77] at the aggregated system level, enabling long-term evaluation of technology transitions. The methodology consists of three main steps:

1. Determination of representative aviation scenarios;
2. Provision of input data and key assumptions;
3. Simulation of aviation scenarios.

Scenario development follows an explorative creation process, including uncertainty–impact and consistency analyses conducted in expert workshops. The fleet model represents the core component of the assessment. It is formulated as a linear programming problem that determines the optimal fleet and fuel type allocation to representative global route pairs over a defined time horizon. To reduce the complexity, aircraft types are clustered into representative categories based on range and seating capacity, and airport pairs are aggregated into representative inter-regional route groups. The system is modeled as a single global airline to capture system-wide transitions rather than competitive airline

behavior. The general overview of the fleet assessment framework can be seen in Figure 27. The mathematical model and the explanation of the model are given in detail in [78].

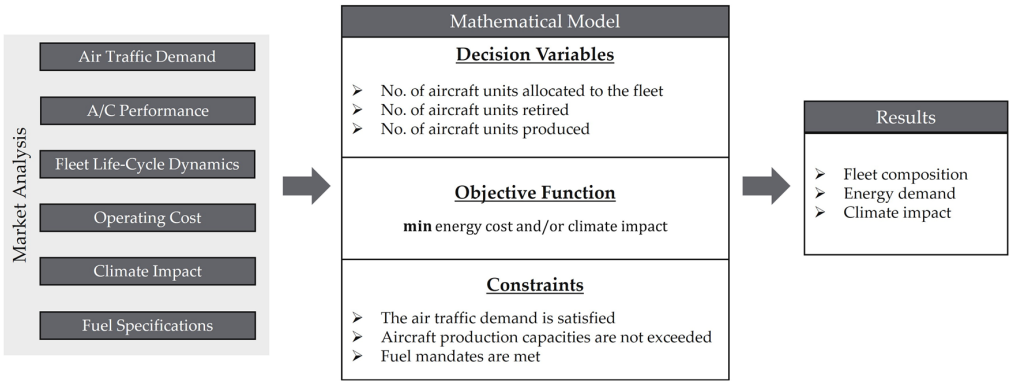


**Figure 27.** Schematic overview of the fleet model.

The model integrates air traffic demand, aircraft performance data, energy-related direct operating cost, climate impact, fleet life-cycle dynamics (aging and retirement), and fuel specifications, including regulatory mandates, as input parameters. The objective function of the model minimizes a weighted combination of the energy component of the direct operating cost and climate impact. The optimization model is subject to several constraints. Demand satisfaction ensures that the available seat capacity on each route pair satisfies the projected air traffic demand in every time period. Production capacity constraint limits the number of newly introduced aircraft per year according to manufacturing capacity restrictions, and fuel mandate constraint enforces that the required share of sustainable aviation fuel is met relative to total conventional fuel consumption in each period. For each scenario, the model provides the evolution of fleet composition, total energy and fuel consumption, and associated climate impact over the assessment horizon at the fleet level.

As described in Section 3 previously, aircraft are grouped into three clusters in this study: regional (REG), short–medium range (SMR), and long-range (LR) aircraft. These aircraft constitute the *reference* fleet and serve as the basis for the development of next-generation *baseline* aircraft as well as *hydrogen* aircraft concepts (Figure 4). Additional aircraft clusters are included in the reference fleet to realistically represent the current global fleet structure based on operational data. The aircraft clusters considered are assessed at the fleet level based on different future scenarios.

All scenarios assume the same passenger demand growth over the analysis horizon (2024–2070) while differing in assumptions regarding aircraft technology introduction, fuel cost developments, and policy measures. The overview of the scenarios used in the study can be seen in Table 12. The reference scenario (S0) represents a continuation of the current technological state in which no new aircraft technologies are introduced and only demand growth affects fleet evolution. The baseline scenario (S1) assumes next-generation conventional aircraft entering service in 2040 with rapid production ramp-up and increasing SAF use driven by the ReFuelEU [79] mandate, while the absence of carbon pricing limits alternative fuel competitiveness and delays hydrogen investments. The hydrogen scenarios (S21 and S22) extend this development through a more ambitious policy framework enabling hydrogen aircraft entry in 2040 and improving liquid hydrogen competitiveness. The two variants differ only in the treatment of non-$CO_2$ effects: S21 excludes contrail impacts, whereas S22 includes them in the climate assessment (see Section 5.1). Additional scenarios are discussed in [78]. The comparison of S1 vs. S21/S22 therefore presents a direct comparison of purely SAF-based and SAF and LH2-based future aviation.

**Table 12.** Overview of scenarios. In the aircraft technology category, values are reported as EIS/qualitative production capacity ramp-up. Fuel costs are expressed as qualitative relative cost levels ($ = low, $$ = medium, and $$$ = high).

| Scenario | S0 (Reference) | S1 (Baseline) | S21 and S22 (Hydrogen) |
|---|---|---|---|
| Aircraft technology | | | |
| Baseline aircraft | – | 2040/rapid ramp-up | 2040/rapid ramp-up |
| Hydrogen aircraft | – | – | 2040/rapid ramp-up |
| Fuel cost assumptions | | | |
| Jet A-1 | $ | $ | $ → $$$ |
| SAF | – | $$$ | $$$ → $$ |
| $LH_2$ | – | – | $$$ → $ |
| Policy framework | | | |
| ReFuelEU mandate | none | yes | yes |
| Carbon tax on Jet A-1 [80,81] | none | none | strong |

The above-mentioned scenarios are translated into model input parameters, and all results in this study are computed by the fleet model for the intermediate weighting of the objective function, which assigns equal importance to energy cost and climate impact.

Figure 28 shows the block energy consumption increases over time in all scenarios due to continued passenger demand growth. However, the baseline scenario (S1) exhibits the lowest block energy consumption, reflecting efficiency improvements from the next-generation baseline aircraft introduced in 2040. In contrast, the hydrogen scenarios (S21 and S22) show slightly higher total block energy consumption after the introduction of hydrogen aircraft in 2040.

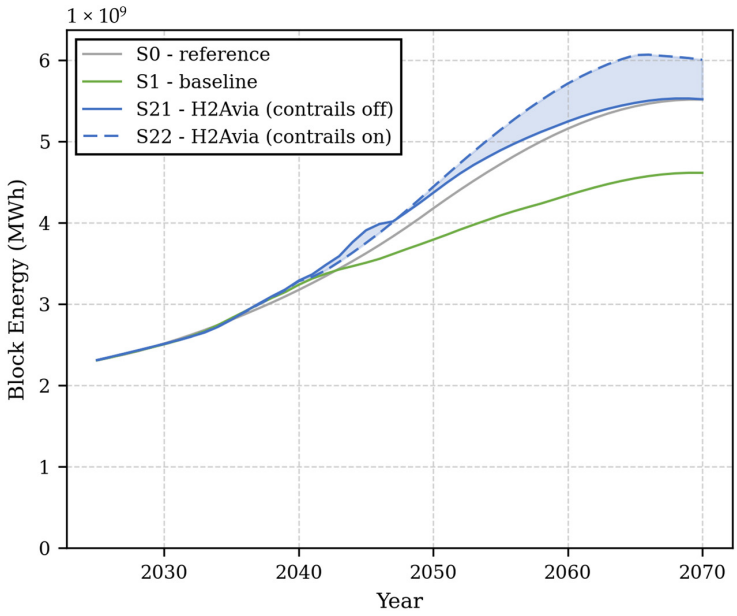


**Figure 28.** Scenario comparison plot over time for total block energy.

Despite this increase in block energy consumption, the climate impact results in Figure 29 indicate a substantial reduction in f-GWP for the hydrogen scenarios compared with S0 and S1. After hydrogen aircraft enter service, f-GWP declines significantly in S21 and S22, with the lowest values observed in S21 (−78% vs. S0 and −60% vs. S1), where contrail effects are not considered, while S22 shows a slightly higher climate impact due to stronger contrail formation. Since S21 and S22 represent two bounding cases for the currently uncertain climate impact of contrails from $H_2$-powered aircraft, they

are not intended to represent equally likely outcomes. S21 assumes negligible contrail effects due to reduced particulate emissions and/or operational mitigation strategies, whereas S22 represents a conservative assumption with persistent contrails and significant climate impact.

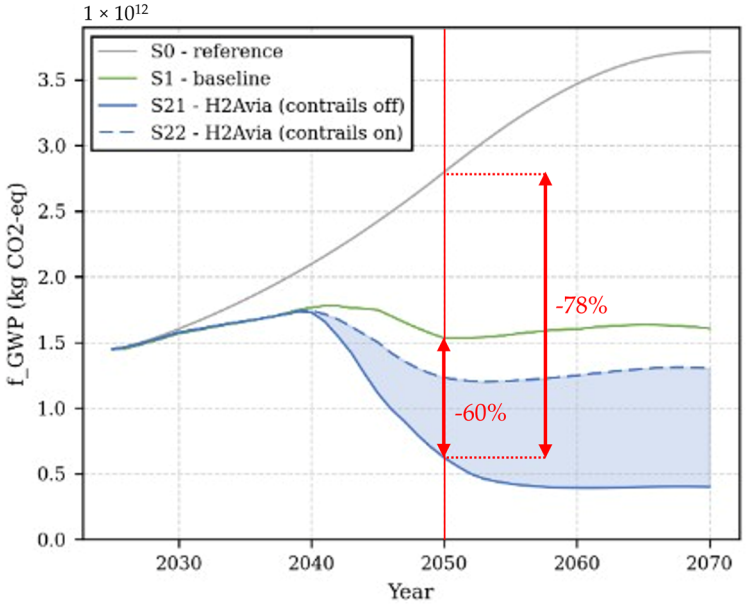


**Figure 29.** Scenario comparison plot over time for total f-GWP.

The transition towards hydrogen aviation is further illustrated by the evolution of energy-based fleet composition over time, as shown in Figure 30 for the hydrogen scenarios S21 and S22. The results indicate that the fleet is initially dominated by conventional aircraft clusters, which gradually decline as they reach the end of their operational lifetime. Following the introduction of hydrogen aircraft in 2040, hydrogen-powered aircraft clusters progressively increase their share of total block and eventually dominate in the later decades of the analysis period. This transition reflects both the production ramp-up of hydrogen aircraft and the gradual retirement of conventional aircraft. While the overall transition pattern is similar in both hydrogen scenarios, the inclusion of contrail effects in S22 slightly influences the timing and magnitude of the fleet transition compared with S21. In the later years of the analysis period (2060–2070), this effect leads to a partial re-introduction of baseline aircraft in S22, resulting in a slight decline in the share of hydrogen-powered aircraft compared with S21.

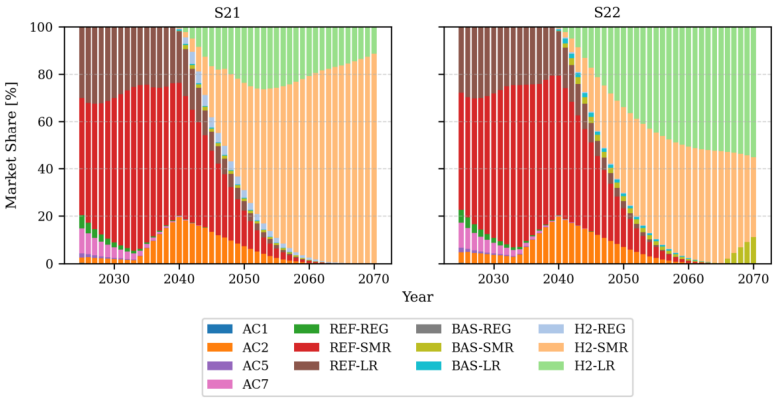


**Figure 30.** Market share of total block energy consumed by aircraft clusters over time for scenario S21 (contrails off, (**left**)) and scenario S22 (contrails on, (**right**)).

## 6. Conclusions and Further Work

Evaluation of the potential of $LH_2$ as an energy carrier requires assessments of complex interactions. The interdisciplinary team of the H2Avia project addressed all main challenges, and the presented research gives a holistic result.

The life-cycle assessment of the production and transport of $LH_2$ was analyzed regarding the impact of different production sites, alongside two renewable electricity production sites, as well as the impact of different transport pathways. Consequently, resulting GWP100 values for $LH_2$ were calculated, including production and transport, as well as $CO_2$ emissions from combustion, resulting in a reduction of 85% compared to conventional jet fuel. The subsequent modeling of aircraft technologies necessary for the operation with $LH_2$ included propulsion, fuel supply system, fuselage $LH_2$ tank integration, dry wings, and an integrated OAD. The propulsion models included adaptations of the thermodynamics modeling for hydrogen combustion and the application of $NO_x$-reducing combustion chamber technologies. The TSPC of the H2 engines compared to the BAS engines showed a reduction of 2–3%, while the $NO_x$ emissions decreased by 70%. For the $LH_2$ fuel system, a component-based approach was applied. The topology of the system included cold boxes and distribution pipes, which were adapted to the aircraft layout. Compared to a conventional kerosene fuel system, a substantial mass increase was found, with the mass of the SMR-H2 fuel system being 1.3 t. The integration of the $LH_2$ tanks in the fuselage was analyzed through a dedicated tool. Hence, the impact of the adapted cabin layouts and fuselage geometries, as well as the effect of the structural integration and loads of the $LH_2$ tanks in the fuselage, could be determined. Analyses for the wing employed aerostructural optimization, identifying wing properties reflecting the targeted EIS 2040 of the BAS and H2 aircraft. A penalty for the expected mass increase of dry wings was applied.

The incorporation of these technologies in an integrated aircraft design yielded the performance comparison on block energy level for the aircraft. The H2 aircraft's design mission block energy increased in comparison to the BAS counterparts, with 13% for the REG, 18% for the SMR, and 8% for the LR. The aircraft mission analysis was executed for multiple payload and range combinations, and the results were processed by a climate impact assessment considering $CO_2$ and non-$CO_2$ effects. The reduction in $f$-GWP100 on the typical missions ranged from 55 to 86% for the different aircraft sizes. Introduction of a global fleet model used an optimization goal incorporating energy cost as well as climate aspects, leading to competition between the BAS and H2 aircraft. For an even weighting of these two goals, the H2 aircraft were mostly more attractive to the fleet model than the BAS aircraft. The resulting reduction in $f$-GWP100 in the year 2050 due to the introduction of the H2 aircraft was 78% compared to the reference scenario and 60% compared to the baseline scenario.

While the presented research incorporated a strongly multi-disciplinary approach, there are still aspects that could extend the scope of such a study.

On the fuel side, the substantial investments required to provide either SAFs or $LH_2$ pose a significant challenge for aviation finances and could inhibit the availability of the required fuel volumes. For this reason, Bauhaus Luftfahrt included this aspect in an interdisciplinary team activity the "Scenario Framework—Aviation 2070". Restrictions on availability could be part of future scenarios and assessments as presented in this paper [82].

Furthermore, the development of aircraft technologies with a currently comparably low maturity, such as the $LH_2$ storage and supply system, will most likely change their respective performance (e.g., in terms of mass). While H2Avia focused only on essential technologies, aircraft incorporating synergistic concepts mitigating the penalties introduced by $LH_2$ on block energy could present a more realistic estimate. An example of ongoing

project is the DWiTE (Dry Wing Technology Exploration) project coordinated by Bauhaus Luftfahrt and propulsion concepts that leverages capabilities unique to $LH_2$ aircraft [83,84].

At a fleet level, the operational costs are strongly dependent on boundary conditions, such as $CO_2$ taxes or mandates driving the use of SAFs. Variations of these could present a corridor of feasible scenarios. Another aspect with strong impact on aviation's climate impact is demand elasticity. While significantly increasing the complexity of the market modeling, operating cost increases due to the transition to non-fossil fuels and the subsequent change in ticket prices and likely transport demand reduction will impact estimates for aviation's future climate impact. $LH_2$ shows a very high potential in aviation and holistic assessments with quantified results should be regularly repeated to sustain and increase the robustness of the statements regarding the advancements in the relevant research areas.

**Author Contributions:** Conceptualization: F.N.P.; Methodology: A.M., C.W., E.E., F.N.P., F.S., L.M., M.E., M.F., M.H. (Mirko Hornung), M.L., N.M., R.B.-X., R.R., S.K., T.B., T.W., V.K.P., and W.H.; Validation: F.N.P., F.S., N.M., and M.L.; Investigation: F.N.P., F.S., L.M., M.F., M.L., N.M., S.K., T.B., T.W., V.K.P., and W.H.; Writing—original draft preparation: A.M., C.W., E.E., E.S., F.N.P., F.S., M.E., M.L., N.M., R.B.-X., S.K., T.B., T.W., and V.K.P.; Writing—review and editing: A.M., A.S., F.N.P., F.S., L.M., M.F., M.L., N.M., R.B.-X., R.R., and V.K.P.; Supervision: A.S., F.N.P., F.S., F.T., and R.R.; Visualization: A.M., E.E., F.N.P., M.E., N.M., R.B.-X., S.K., T.W., T.B., and V.K.P.; Project administration: F.N.P.; Funding acquisition: A.S., E.S., F.N.P., F.S., F.T., M.H. (Matthias Haupt), N.M., and R.R. All authors have read and agreed to the published version of the manuscript.

**Funding:** H2Avia was a project of the German federal funded aviation research program (LuFo) VI-2FKZ 20E2106.

**Data Availability Statement:** The original contributions presented in this study are included in this article. Further inquiries should be directed to the corresponding author.

**Acknowledgments:** We would like to thank the following colleagues for their support of H2Avia. Former employees of the project partners: Benjamin Portner (BHL), Julia Schaumeier (BHL), Kathrin Ebner (BHL), Markus Nickl (BHL), Ralph Stephan (RWTH), and Thomas Maibach (TUHH).

**Conflicts of Interest:** The authors declare no conflicts of interest. The funders had no role in the design of the study; in the collection, analyses, or interpretation of data; in the writing of the manuscript; or in the decision to publish the results.

## Abbreviations

The following abbreviations are used in this manuscript:

| | |
|---|---|
| AIC | Aviation-Induced Cloudiness |
| APU | Auxiliary Power Unit |
| AtJ | Alcohol-to-Jet |
| ATR | Average Temperature Response |
| BLADE | Bauhaus Luftfahrt Aircraft Design Environment |
| BPR | Bypass Ratio |
| CAFE | Cabin and Fuselage Design Environment |
| CFRPs | Carbon Fiber Reinforced Plastics |
| CG | Center of Gravity |
| CPACS | Common Parametric Aircraft Configuration Schema |
| ECS | Environmental Control System |
| EIS | Entry Into Service |
| $f$-GWP | Efficacy-Weighted Global Warming Potential |
| FLHYTE | Fuselage Design and Hydrogen Tank Integration Tool Environment |

| | |
|---|---|
| $FN_{ST}$ | Net Static Thrust |
| GH2 | Gaseous Hydrogen |
| GHI | Global Horizontal Irradiation |
| GI | Gravimetric Index |
| GWP | Global Warming Potential |
| HEFA | Hydroprocessed Esters And Fatty Acids |
| HyDRA | Hydrogen Tank Design Routine and Assessment |
| ISA | International Standard Atmosphere |
| L/D | Lift-to-Drag Ratio |
| LCA | Life-Cycle Assessment |
| $LH_2$ | Liquid Hydrogen |
| LR-BAS | Long-Range Baseline Aircraft |
| LR-H2 | Long-Range Hydrogen Aircraft |
| LR-REF | Long-Range Reference Aircraft |
| MCL | Maximum Climb |
| MDO | Multi-Disciplinary Optimization |
| MTOM | Maximum Take-Off Mass |
| OAD | Overall Aircraft Design |
| OBSs | On-Board Systems |
| OME | Operating Mass Empty |
| OPR | Overall Pressure Ratio |
| OSD | Overall Systems Design |
| PrADO | Preliminary Aircraft Design and Optimisation Program |
| PtL | Power-to-Liquid |
| REG-BAS | Regional-Range Baseline Aircraft |
| REG-H2 | Regional-Range Hydrogen Aircraft |
| REG-REF | Regional-Range Reference Aircraft |
| RF | Radiative Forcing |
| SAF | Sustainable Aviation Fuel |
| SArA | Systems Architecting Assistant |
| SL | Sea Level |
| SMR-BAS | Short–Medium-Range Baseline Aircraft |
| SMR-H2 | Short–Medium-Range Hydrogen Aircraft |
| SMR-REF | Short–Medium-Range Reference Aircraft |
| T4 | Turbine Inlet Temperature |
| TLARs | Top-Level Aircraft Requirements |
| ToC | Top of Climb |
| TSFC | Thrust Specific Fuel Consumption |
| TSPC | Thrust Specific Power Consumption |
| UNICADO | University Conceptual Aircraft Design and Optimization |

## References

1. Peter, F.N. *Verbundbeschreibung des Verbundvorhaben H2Avia—Hydrogen in Aviation: Förderantrag im Rahmen der Luftfahrtforschung und–Technologie LuFoVI-2*; Bauhaus Luftfahrt: Taufkirchen, Germany, 2021.
2. Peter, F.N.; Habersetzer, A.; Nickl, M.; Lüdemann, M.; Ebner, K.; Effing, T.; Badrya, C.; Haupt, M.; Jünemann, M.; Möbs, N. *H2Avia—Project Description*; Bauhaus Luftfahrt: Taufkirchen, Germany, 2023.
3. Peter, F.N.; Xicohténcatl, R.B.; Engelmann, M.; Fikry, M.; Lüdemann, M.; Muslic, A.; Stephan, R.; Kakkar, S.; Maibach, T.; Moebs, N. The H2Avia Project—Goals and Aircraft Synthesis Strategy. In *Proceedings of the 14th EASN International Conference on "Innovation in Aviation & Space for Opening New Horizons", Thessaloniki, Greece, 8–11 October 2024*; EASN (The European Aeronautics Science Network), Ed.; EASN: Brussels, Belgium, 2024.
4. Sosounov, V.; Orlov, V. Experimental turbofan using liquid hydrogen and liquid natural gas as fuel. In *Proceedings of the 26th Joint Propulsion Conference, Orlando, FL, USA, 16–18 July 1990*; AIAA (The American Institute of Aeronautics and Astronautics), Ed.; American Institute of Aeronautics and Astronautics: Reston, VA, USA, 1990.
5. Brewer, G.D. *Hydrogen Aircraft Technology*, 1st ed.; CRC Press: Boca Raton, FL, USA, 1991; ISBN 9781351439787.

6. EU Research. *Liquid Hydrogen Fuelled Aircraft—System Analysis: (Publishable Version)*; Final Technical Report Project No. G4RD-CT-2000-00192; EU: Brussels, Belgium, 2003.
7. Huete, J.; Pilidis, P. Parametric study on tank integration for hydrogen civil aviation propulsion. *Int. J. Hydrogen Energy* **2021**, *46*, 37049–37062. [CrossRef]
8. Onorato, G.; Proesmans, P.; Hoogreef, M.F.M. Assessment of hydrogen transport aircraft. *CEAS Aeronaut. J.* **2022**, *13*, 813–845. [CrossRef] [PubMed]
9. Patrao, A.C.; Jonsson, I.; Xisto, C.; Lundbladh, A.; Grönstedt, T. Compact heat exchangers for hydrogen-fueled aero engine intercooling and recuperation. *Appl. Therm. Eng.* **2024**, *243*, 122538. [CrossRef]
10. Ramm, J.; Rahn, A.; Silberhorn, D.; Wicke, K.; Wende, G.; Papantoni, V.; Linke, F.; Kühlen, M.; Dahlmann, K. Assessing the Feasibility of Hydrogen-Powered Aircraft: A Comparative Economic and Environmental Analysis. *J. Aircr.* **2024**, *61*, 1337–1353. [CrossRef]
11. Airbus. ZEROe: Our Hydrogen-Powered Aircraft. Available online: https://www.airbus.com/en/innovation/energy-transition/hydrogen/zeroe-our-hydrogen-powered-aircraft (accessed on 22 May 2026).
12. Fokker Next Gen. Fokker Next Gen: Engineering a New Aeronautical Experience. Available online: https://www.fokkernextgen.com/the-aircraft (accessed on 21 November 2025).
13. Cole, J.; McClintock, W.; Powis, L. *Market Forecast & Strategy*; FlyZero FZO-CST-REP-0043; FlyZero: Bedford, UK, 2022.
14. Moser, L.; Portner, B.W.; Penke, C.; Ebner, K.; Batteiger, V. Life-Cycle assessment of renewable fuel production via hydrothermal liquefaction of manure in Germany. *Sustain. Energy Fuels* **2023**, *7*, 4898. [CrossRef]
15. Global Wind Atlas: Global Solaratlas, Energydata.info. Available online: https://globalwindatlas.info/en (accessed on 11 June 2024).
16. Solargis. Global Solar Atlas. Available online: https://globalsolaratlas.info/map?c=30.387092,-7.174072,7&s=31.118794,-6.580811&m=site (accessed on 5 March 2026).
17. Petra, I.; Thomas, L. *Entwicklung der Spezifischen Treibhausgas-Emissionen des Deutschen Strommix in den Jahren 1990–2024*; Umweltbundesamt: Dessau-Roßlau, Germany, 2025.
18. Schloemer, S.; Bruckner, T.; Fulton, L.; Hertwich, E.; McKinnon, A.; Perczyk, D.; Roy, J.; Schaeffer, R.; Sims, R.; Smith, P.; et al. Annex III: Technology-specific cost and performance parameters. In *Climate Change 2014: Mitigation of Climate Change: Contribution of Working Group III to the Fifth Assessment Report of the Intergovernmental Panel on Climate Change*; Cambridge University Press: Cambridge, UK; New York, NY, USA, 2014; pp. 1329–1356.
19. Micheli, M.; Moore, D.; Bach, V.; Finkbeiner, M. Life-Cycle Assessment of Power-to-Liquid Kerosene Produced from Renewable Electricity and CO2 from Direct Air Capture in Germany. *Sustainability* **2022**, *14*, 10658. [CrossRef]
20. Rojas-Michaga, M.F.; Michailos, S.; Cardozo, E.; Akram, M.; Hughes, K.J.; Ingham, D.; Pourkashanian, M. Sustainable aviation fuel (SAF) production through power-to-liquid (PtL): A combined techno-economic and life cycle assessment. *Energy Convers. Manag.* **2023**, *292*, 117427. [CrossRef]
21. Treyer, K.; Sacchi, R.; Bauer, C. *Life Cycle Assessment of Synthetic Hydrocarbons for Use as Jet Fuel: "Power-to-Liquid" and "Sun-to-Liquid" Processes*; Paul Scherrer Institute: Würenlingen, Switzerland, 2022.
22. ICAO (The International Civil Aviation Organization). *CORSIA Default Life Cycle Emissions Values for CORSIA Eligible Fuels*; ICAO: Montreal, QC, Canada, 2025.
23. Fesmire, J.E.; Swanger, A. Overview of the New LH2 Sphere at NASA Kennedy Space Center. Available online: https://www.energy.gov/sites/default/files/2021-10/new-lh2-sphere.pdf (accessed on 22 February 2023).
24. Hoelzen, J.; Flohr, M.; Silberhorn, D.; Mangold, J.; Bensmann, A.; Hanke-Rauschenbach, R. H2-powered aviation at airports—Design and economics of LH2 refueling systems. *Energy Convers. Manag. X* **2022**, *14*, 100206. [CrossRef]
25. Petitpas, G. *Boil-off Losses Along LH2 Pathway*; LLNL-TR-750685; Lawrence Livermore National Laboratory: Livermore, CA, USA, 2018. [CrossRef]
26. Restelli, F.; Jiao, F.; Norris, B.; Trusler, J.M.; Siahvashi, A.; May, E.F.; Pellegrini, L.A.; Johns, M.; Al Ghafri, S.Z. Dynamic simulation of a liquefied hydrogen export terminal. *Energy* **2026**, *342*, 139715. [CrossRef]
27. Zimmnau, M.; Schültke, F.; Stumpf, E. UNICADO: Multidisciplinary analysis in conceptual aircraft design. *CEAS Aeronaut. J.* **2023**, *14*, 75–89. [CrossRef]
28. Barnert, M.; Schültke, F.; Stumpf, E. Design of a low-emission long-range aircraft using UNICADO. *CEAS Aeronaut. J.* **2026**. [CrossRef]
29. Risse, K.; Schäfer, K.; Schültke, F.; Stumpf, E. Central Reference Aircraft data System (CeRAS) for research community. *CEAS Aeronaut. J.* **2016**, *7*, 121–133. [CrossRef]
30. Boundy, R.; Diegel, S.; Wright, L.; Davis, S. *Biomass Energy Data Book*, 4th ed.; U.S. Department of Energy: Washington, DC, USA, 2011.
31. Mcbride, B.J.; Gordon, S. *Computer Program for Calculation of Complex Chemical Equilibrium Compositions and Applications. Part 2: Users Manual and Program Description*; NASA: Washington, DC, USA, 1976.

32. Martin, S.; Sebastian, B. *Overview on Fuel Flow Correlation Methods for the Calculation of NOx, CO and HC Emissions and Their Implementation into Aircraft Performance Software*; Institut für Antriebstechnik: Cologne, Germany, 2013.
33. Sáez Ortuño, M.Á.; Yin, F.; Gangoli Rao, A.; Vos, R.; Proesmans, P.-J. Climate Assessment of Hydrogen Combustion Aircraft: Towards a Green Aviation Sector. In *AIAA SCITECH 2023 Forum*; American Institute of Aeronautics and Astronautics: Reston, VA, USA, 2023.
34. Seitz, A.; Schmitz, O.; Isikveren, A.T.; Hornung, M. Electrically Powered Propulsion: Comparison and Contrast to Gas Turbines. In *Proceedings of the Deutscher Luft- und Raumfahrtkongress (DLRK), Berlin, Germany, 10–12 September 2012*; DGLR (Deutsche Gesellschaft für Luft- und Raumfahrt), Ed.; DGLR: Bonn, Germany, 2012.
35. Meissner, R.; Sieb, P.; Wollenhaupt, E.; Haberkorn, S.; Wicke, K.; Wende, G. Towards climate-neutral aviation: Assessment of maintenance requirements for airborne hydrogen storage and distribution systems. *Int. J. Hydrogen Energy* **2023**, *48*, 29367–29390. [CrossRef]
36. Nils, K.; Jasmin, B.; Thimo, B.; Frank, T. Systems Architecting Assistant (SARA)—Enabling a Seamless Process Chain from Requirements to Overall Systems Design. In Proceedings of the 33rd Congress of the International Council of the Aeronautical Science, Stockholm, Sweden, 4–9 September 2022.
37. Bielsky, T.; Kuelper, N.; Thielecke, F. Assessment of an auto-routing method for topology generation of aircraft power supply systems. *CEAS Aeronaut. J.* **2024**, *15*, 765–779. [CrossRef]
38. Juenemann, M.; Kriewall, V.; Bielsky, T.; Thielecke, F. Overall Systems Design Method for Evaluation of Electro-Hydraulic Power Supply Concepts for Modern Mid-Range Aircraft. In *Proceedings of the AIAA Aviation 2022 Forum, Chicago, IL, USA & Virtual, 27 June–1 July 2022*; AIAA (The American Institute of Aeronautics and Astronautics): Reston, VA, USA, 2022.
39. Thimo, B.; Nils, K.; Frank, T. Overall Parametric Design and Integration of On-Board Systems for a Hydrogen-Powered Concept Aircraft. In *Proceedings of the Aerospace Europe Conference 2023*; EUCASS: Brussels, Belgium, 2023.
40. Alder, M.; Moerland, E.; Jepsen, J.; Nagel, B. Recent Advances in Establishing a Common Language for Aircraft Design with CPACS. In *Proceedings of the Aerospace Europe Conference 2020*; EUCASS: Brussels, Belgium, 2020.
41. Burschyk, T.; Alder, M.; Mancini, A.; Bielsky, T.; Kriewall, V.; Thielecke, F.; Nagel, B. Introduction of a System Definition in the Common Parametric Aircraft Configuration Schema (CPACS). *Aerospace* **2025**, *12*, 373. [CrossRef]
42. Bielsky, T.; Gossel, J.; Thielecke, F. Evaluation of Interdependencies between the Hydrogen Supply System and the Electrical Supply System for Aircraft Conceptual Design. In *Proceedings of the Deutscher Luft- und Raumfahrtkongress 2023*; DGLR: Bonn, Germany, 2024.
43. Fesmire, J.E. Aerogel insulation systems for space launch applications. *Cryogenics* **2006**, *46*, 111–117. [CrossRef]
44. Engelmann, M.; Lüdemann, M.; Peter, F.N. Cabin And Fuselage Design For The H2Avia Hydrogen Aircraft Concepts. In *Proceedings of the 73. Deutscher Luft- und Raumfahrtkongress (DLRK), Hamburg, Germany, 30 September–2 October 2024*; DGLR (Deutsche Gesellschaft für Luft- und Raumfahrt), Ed.; DGLR: Bonn, Germany, 2024.
45. Lüdemann, M.; Engelmann, M.; Kellermann, H.; Maas, P.; Peter, F.; Hornung, M.; Troeltsch, F. BLADE: A Modular Environment for Traceable and Automated Aircraft Design. In Proceedings of the 13th EASN International Conference 2023, Salerno, Italy, 6 September 2023.
46. Engelmann, M.; Hornung, M. Geometric optimization of hydrogen aircraft fuselages in preliminary design. In Proceedings of the 34th Congress of the International Council of the Aeronautical Sciences, Florence, Italy, 9–13 September 2024.
47. American Bureau of Shipping. Guidance Notes on Strength Assessment of Independent Type C Tanks. Available online: https://ww2.eagle.org/content/dam/eagle/rules-and-guides/current/design_and_analysis/327_gn_type_C_tanks_2022/type-c-tanks-gn-jan22.pdf (accessed on 1 February 2026).
48. Hellbrück, S.; Hesse, C.; Bielsky, T.; Thielecke, F.; Biedermann, J.; Nagel, B. Knowledge-based engineering methods for hydrogen tank and system integration in aircraft fuselage design. *CEAS Aeronaut. J.* **2026**. [CrossRef]
49. Ardema, M.D.; Chambers, M.C.; Patron, A.P. *Analytical Fuselage and Wing Weight Estimation of Transport Aircraft*; NASA Technical Memorandum No. 110392; NASA: Washington, DC, USA, 1996.
50. Sudhi, A.; Radespiel, R.; Badrya, C. Design Exploration of Transonic Airfoils for Natural and Hybrid Laminar Flow Control Applications. *J. Aircr.* **2023**, *60*, 716–732. [CrossRef]
51. Österheld, C.M. *Physikalisch Begründete Analyseverfahren im Integrierten Multidisziplinären Flugzeugvorentwurf*; Shaker: Aachen, Germany, 2004.
52. Heinze, W.; Österheld, C.M.; Horst, P. Multidisziplinäres Flugzeugentwurfsverfahren PrADO—Programmentwurf und Anwendung im Rahmen von Flugzeug-Konzeptstudien. In *Proceedings of the Deutscher Luft- und Raumfahrtkongress (DLRK), Bremen, Germany, 31 August–2 September 2021*; DGLR (Deutsche Gesellschaft für Luft- und Raumfahrt), Ed.; DGLR: Bonn, Germany, 2021.
53. Rieke, J. *Bewertung von CFK-Strukturen in Einem Multidisziplinären Entwurfsansatz für Verkehrsflugzeuge*; Cuvillier: Göttingen, Germany, 2013.

54. Fornasier, L. HISSS—A higher-order subsonic/supersonic singularity method for calculating linearized potential flow. In *Proceedings of the 17th Fluid Dynamics, Plasma Dynamics, and Lasers Conference, Snowmass, CO, USA, 25–27 June 1984*; American Institute of Aeronautics and Astronautics, Ed.; American Institute of Aeronautics and Astronautics: Reston, VA, USA, 1984.
55. Garnett, R. *Bayesian Optimization*; Cambridge University Press: Cambridge, UK, 2023.
56. Kakkar, S.; Heinze, W.; Haupt, M.; Sudhi, A.; Badrya, C.; Radespiel, R. Aerostructural Optimisation of Dry Wings for Hydrogen Aircraft. In *Proceedings of the 73. Deutscher Luft- und Raumfahrtkongress (DLRK), Hamburg, Germany, 30 September–2 October 2024*; DGLR (Deutsche Gesellschaft für Luft- und Raumfahrt), Ed.; DGLR: Bonn, Germany, 2024.
57. Phillips, W.F.; Hunsaker, D.F.; Joo, J.J. Minimizing Induced Drag with Lift Distribution and Wingspan. *J. Aircr.* **2019**, *56*, 431–441. [CrossRef]
58. Airbus Canada Limited Partnership. *Airbus A220 Aircraft Characteristics Publication ACP*; BD500-3AB48-13800-00, Issue No. 001; Airbus: Leiden, The Netherlands, 2023.
59. EASA (The European Union Aviaton Safety Agency). *Type-Certificate Data Sheet, No. EASA.A.064 for AIRBUS A318–A319–A320–A321*; Issue 60; EASA: Cologne, Germany, 2025.
60. EASA (The European Union Aviaton Safety Agency). *Type-Certificate Data Sheet for Airbus A350*; TCDS EASA.A.151, Issue 32; EASA: Cologne, Germany, 2025.
61. Catalano, P.; de Rosa, D.; Mele, B.; Tognaccini, R.; Moens, F. Performance Improvements of a Regional Aircraft by Riblets and Natural Laminar Flow. *J. Aircr.* **2020**, *57*, 29–40. [CrossRef]
62. Weber, L.; Szöke-Erös, H.; Ratei, P.; Shiva Prakasha, P. A Technlogy Scouting and Roadmapping Approach of Future Commercial Passenger Aircraft. In *Proceedings of the Deutscher Luft- und Raumfahrtkongress 2024*; DGLR: Bonn, Germany, 2024.
63. Niu, M.C.-Y. *Airframe Structural Design: Practical Design Information and Data on Aircraft Structures*, 2nd ed.; Conmilit Press: Hong Kong, China, 2002.
64. Torenbeek, E. *Development and Application of a Comprehensive, Design-Sensitive Weight Prediction Method for Wing Structures of Transport Category Aircraft*; Report LR-693; Delft University of Technology: Delft, The Netherlands, 1992.
65. Jenkinson, L.R.; Simpkin, P.; Rhodes, D. *Civil Jet Aircraft Design*; Arnold: London, UK, 1999.
66. Kotzem, M.; Wöhler, S.; Burschyk, T.; Hesse, C.; Hellbrück, S.; Zill, T. Conceptual Aircraft Design of a Research Baseline with Direct Liquid Hydrogen Combustion. In *Proceedings of the 34th Congress of the International Council of the Aeronautical Sciences, ICAS 2024*; ICAS: Bonn, Germany, 2024.
67. Turner, J.; Contaut, S. *Cryogenic Hydrogen Fuel System and Storage Roadmap: FlyZero*. FZO-PPN-COM-0027. 2022. Available online: https://www.ati.org.uk/wp-content/uploads/2022/03/FZO-PPN-COM-0027-Cryogenic-Hydrogen-Fuel-System-and-Storage-Roadmap-Report.pdf (accessed on 1 June 2026).
68. Sausen, R.; Schumann, U. *Estimates of the Climate Response to Aircraft Emissions Scenarios*; Report No. 95; Institut fur Physik der Atmosphare: Weßling, Germany, 1998.
69. Grewe, V.; Stenke, A. AirClim: An efficient tool for climate evaluation of aircraft technology. *Atmos. Chem. Phys.* **2008**, *8*, 4621–4639. [CrossRef]
70. Dallara, E.S.; Kroo, I.M.; Waitz, I.A. Metric for Comparing Lifetime average Climate Impact of Aircraft. *AIAA J.* **2011**, *49*, 1600–1613. [CrossRef]
71. Wiegand, M.; Koops, L.; Mailach, R.; Balderas-Xicohtencatl, R. Uncertainty Quantification in Aviation Climate Impact: A Stochastic Approach to $CO_2$ and Non-$CO_2$ Effects. *Research Square* **2026**. [CrossRef]
72. Lee, D.S.; Fahey, D.W.; Skowron, A.; Allen, M.R.; Burkhardt, U.; Chen, Q.; Doherty, S.J.; Freeman, S.; Forster, P.M.; Fuglestvedt, J.; et al. The contribution of global aviation to anthropogenic climate forcing for 2000 to 2018. *Atmos. Environ.* **2021**, *244*, 117834. [CrossRef]
73. Bier, A.; Unterstrasser, S.; Zink, J.; Hillenbrand, D.; Jurkat-Witschas, T.; Lottermoser, A. Contrail formation on ambient aerosol particles for aircraft with hydrogen combustion: A box model trajectory study. *Atmos. Chem. Phys.* **2024**, *24*, 2319–2344. [CrossRef]
74. Megaritis, T. *Influence of Aviation Fuel Composition on the Formation and Lifetime of Contrails—A Literature Review*; Concawe: Brussels, Belgium, 2024.
75. Lottermoser, A.; Unterstraßer, S. High-resolution modeling of early contrail evolution from hydrogen-powered aircraft. *Atmos. Chem. Phys.* **2025**, *25*, 7903–7924. [CrossRef]
76. Köhler, M.O.; Rädel, G.; Dessens, O.; Shine, K.P.; Rogers, H.L.; Wild, O.; Pyle, J.A. Impact of perturbations to nitrogen oxide emissions from global aviation. *J. Geophys. Res. Atmos.* **2008**, *113*. [CrossRef]
77. Belobaba, P.P.; Odoni, A.; Barnhart, C. (Eds.) *The Global Airline Industry*, 1st ed.; John Wiley & Sons: New York, NY, USA, 2009.
78. Muslić, A.; Erden, E.; Balderas-Xicohtencatl, R.; Peter, F.N.; Hornung, M. Fleet-Level Assessment of Hydrogen-Powered Aircraft Using Scenario-Based Modeling. *Aerospace* **2026**, *13*, 517. [CrossRef]
79. EU. *Regulation (EU) 2023/2405 of the European Parliament and of the Council of 18 October 2023 on Ensuring a Level Playing Field for Sustainable air Transport (ReFuelEU Aviation)*; ReFuelEU Aviation; EU: Brussels, Belgium, 2023.

80. International Renewable Energy Agency. *Accelerating Hydrogen Deployment in the G7-Recommendations for the Hydrogen Action Pact*; International Renewable Energy Agency IRENA: Abu Dhabi, United Arab Emirates, 2022.
81. van Velzen, A. *Environmental and Economic Impacts of EU ETS and CORSIA Policy Scenarios for European Aviation: Report Prepared by TAKS for Transport and Environment (T&E) and Carbon Market Watch (CMW)*; Report nr: 22-11; TAKS: Utrecht, The Netherlands, 2022.
82. Bauhaus Luftfahrt. *Bauhaus Luftfahrt Yearbook 2025*; Bauhaus Luftfahrt: Taufkirchen, Germany, 2026. Available online: https://www.bauhaus-luftfahrt.net/epdf/Bauhaus-Luftfahrt-E-Jahrbuch-2025/#0 (accessed on 1 June 2026).
83. Seitz, A. *Propulsion Technology Options for Climate-Compliant Aircraft Design*; Bauhaus Luftfahrt: Taufkirchen, Germany, 2024.
84. Seitz, A.; Nickl, M.; Troeltsch, F.; Ebner, K. Initial Assessment of a Fuel Cell—Gas Turbine Hybrid Propulsion Concept. *Aerospace* **2022**, *9*, 68. [CrossRef]